XSHOOTER spectroscopy of the enigmatic planetary nebula Lin49 in the Small Magellanic Cloud

Monthly Notices
of the
ROYAL ASTRONOMICAL SOCIETY

MNRAS **462,** 12–34 (2016)
Advance Access publication 2016 July 11

doi:10.1093/mnras/stw1615

XSHOOTER spectroscopy of the enigmatic planetary nebula Lin49 in the Small Magellanic Cloud

Masaaki Otsuka,[1]★ F. Kemper,[1] M. L. Leal-Ferreira,[2]† I. Aleman,[2] J. Bernard-Salas,[3] J. Cami,[4,5] B. B. Ochsendorf,[2,6] E. Peeters[4,5] and P. Scicluna[1]

[1]*Academia Sinica, Institute of Astronomy and Astrophysics, 11F Astronomy-Mathematics Building, NTU/AS campus, No. 1, Section 4, Roosevelt Rd., Taipei 10617, Taiwan, Republic of China*
[2]*Leiden Observatory, University of Leiden, PO Box 9513, NL-2300 RA, Leiden, the Netherlands*
[3]*Department of Physical Sciences, The Open University, Milton Keynes MK7 6AA, UK*
[4]*Department of Physics and Astronomy, The University of Western Ontario, London, ON N6A 3K7, Canada*
[5]*SETI Institute, 189 Bernardo Ave, Suite 100, Mountain View, CA 94043, USA*
[6]*Department of Physics and Astronomy, The Johns Hopkins University, 3400 North Charles Street, Baltimore, MD 21218, USA*

Accepted 2016 July 4. Received 2016 July 1; in original form 2016 February 23

ABSTRACT

We performed a detailed spectroscopic analysis of the fullerene C_{60}-containing planetary nebula (PN) Lin49 in the Small Magellanic Cloud (SMC) using XSHOOTER at the European Southern Observatory Very Large Telescope and the *Spitzer*/Infrared Spectrograph instruments. We derived nebular abundances for nine elements. We used TLUSTY to derive photospheric parameters for the central star. Lin49 is C-rich and metal-deficient PN ($Z \sim 0.0006$). The nebular abundances are in good agreement with asymptotic giant branch nucleosynthesis models for stars with initial mass 1.25 $M_{\odot}$ and metallicity $Z = 0.001$. Using the TLUSTY synthetic spectrum of the central star to define the heating and ionizing source, we constructed the photoionization model with CLOUDY that matches the observed spectral energy distribution (SED) and the line fluxes in the UV to far-IR wavelength ranges simultaneously. We could not fit the ∼1–5 μm SED using a model with 0.005–0.1-μm-sized graphite grains and a constant hydrogen density shell owing to the prominent near-IR excess, while at other wavelengths the model fits the observed values reasonably well. We argue that the near-IR excess might indicate either (1) the presence of very small particles in the form of small carbon clusters, small graphite sheets, or fullerene precursors, or (2) the presence of a high-density structure surrounding the central star. We found that SMC C_{60} PNe show a near-IR excess component to lesser or greater degree. This suggests that these C_{60} PNe might maintain a structure nearby their central star.

Key words: ISM: abundances – dust, extinction – planetary nebulae: individual: Lin49.

1 INTRODUCTION

The discovery of C_{60} in the C-rich planetary nebula (PN) Tc1 (Cami et al. 2010) confirmed the presence outside the Solar system of the enigmatic molecule buckminsterfullerene C_{60}, first discovered by Kroto et al. (1985). Since then, C_{60} has been identified towards 10 other PNe in the Milky Way (MW; Cami et al. 2010; García-Hernández et al. 2010, 2011, 2012; Otsuka et al. 2013, 2014), bringing the total to 11 detections out of a sample of 338, both C-rich and O-rich, PNe observed with the Infrared Spectrograph (IRS; Houck et al. 2004) on the *Spitzer Space Telescope*. Assuming that the evolved star content of the MW is 1/3 C-rich and 2/3 O-rich (Ishihara et al. 2011), it can be inferred that fullerenes occur in about 10 per cent of the Galactic C-rich PNe, although this number may be lower if a larger fraction of Galactic PNe are C-rich. For C-rich PNe, Garcia-Hernandez (2015) reports a detection rate of ∼5 per cent, ∼20 per cent, and ∼44 per cent in the MW, the Large Magellanic Cloud (LMC), and Small Magellanic Cloud (SMC), respectively. This indicates that the processing of fullerenes may depend on the metallicity, with fullerenes being more often detected in low-metallicity environments. In most cases, even the two strongest C_{60} resonances at 17.4 and 18.9 μm are rather weak with respect to the local continuum emission around these wavelengths, with the notable exception of the PN Lin49 (Fig. 1) in the SMC, which appears to have C_{60} 17.4 and 18.9 μm features of very similar strength and appearance to what is seen towards Tc1. The similarities

★ E-mail: otsuka@asiaa.sinica.edu.tw
† CNPq/Brazil Fellow.

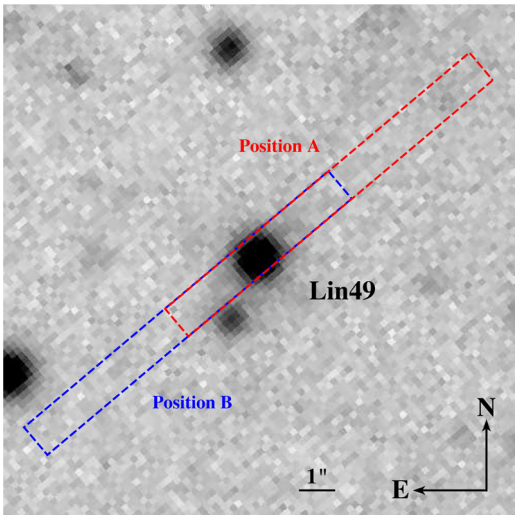

Figure 1. Image of Lin49 in the z' band and the slit positions used in the XSHOOTER observations. We observed Lin49 on the slit positions A and B. The averaged FWHM amongst nine nearby stars is ∼0.69 arcsec.

in their infrared spectra and the similar C_{60} band strengths motivated us to know more about physical properties of Lin49.

However, little is known about Lin49. Prior to its *Spitzer*/IRS observation, Lin49 only occurs in some catalogues as an SMC PN (Lindsay 1961; Dopita et al. 1985; Meyssonnier & Azzopardi 1993; Morgan 1995) until recently. The source was selected for spectroscopic follow-up with *Spitzer* based on its mid-infrared (mid-IR) Infrared Array Camera (IRAC) photometric colours, which suggested a pre-main-sequence nature (Sloan, private communication). The *Spitzer*/IRS spectrum revealed that Lin49 is a C-rich dust PN, showing strong C_{60} resonances at 17.4 and 18.9 μm and similar dust features such as the broad 11 and 30 μm bands seen in the other C_{60}-containing LMC and SMC PNe (Sloan et al. 2014; Ruffle et al. 2015), but the physical properties of the central star and dusty nebula remain unknown. Therefore, we wanted to further characterize Lin49 using the XSHOOTER UV–near-IR (NIR) spectrograph (Vernet et al. 2011) on the European Southern Observatory (ESO) Very Large Telescope (VLT) UT2 (Kueyen), in combination with the *Spitzer*/IRS spectrum. In the case of Lin49, the well-determined distance to the SMC allows us to accurately determine the luminosity of the central star, the size of the nebula, and the total gas and dust masses in the nebula, and then clarify the current evolutionary stage of the central star and estimate the initial mass.

In this study, we present a spectroscopic analysis of Lin49 in order to study the physical conditions and chemical properties of this interesting PN. This is part of an ongoing study to understand in more depth the physical and chemical properties of fullerene-containing PNe. Although we expect that these studies give us information on why fullerenes formed and exist in these PNe, the aim of this specific paper is not to investigate the formation and processing of fullerene molecules.

The remainder of this paper is organized as follows. In Section 2, we describe our XSHOOTER observation and the data reduction of the XSHOOTER spectrum and the archived *Spitzer*/IRS spectrum. The results of plasma-diagnostic and ionic and elemental abundance derivations using nebular lines, derivations of photospheric properties, and spectral energy distribution (SED) fitting are described in Section 3. In Section 4, we discuss the prominent NIR excess found in Lin49, and we give interpretations of this feature. We discuss the SEDs of SMC C_{60} PNe and non-C_{60} C-rich PNe in the SMC by comparing with the SED of Lin49. We compare physical properties of the C_{60}-containing PNe and counterparts in the SMC. Finally, we summarize the works in Section 5.

2 OBSERVATIONS AND DATA REDUCTIONS

2.1 ESO/VLT XSHOOTER spectroscopy

We obtained a UV to NIR spectrum using the medium-resolution spectrograph XSHOOTER, attached to the Cassegrain focus of the 8.2 m VLT UT2 at the ESO Paranal observatory, in Chile, on 2013 July 17 (UT). The XSHOOTER instrument consists of three spectroscopic arms: UVB, VIS, and NIR; and it covers the wavelength range from 2936 to 24 800 Å. The weather conditions during the exposure were stable, and the seeing recorded in the Differential Image Motion Monitor seeing monitor was ∼0.65–1.04 arcsec. For the UVB and VIS arms, we inserted the atmospheric dispersion correctors in front of the slits in order to minimize the differential atmospheric dispersion throughout the broad wavelength range. We used a slit size of 1.0 arcsec×11 arcsec in the UVB arm and 0.9 arcsec×11 arcsec in the other arms. We selected the 1×1 binning mode in each detector. The difference of the slit width in each arm[1] and the difference of plate scale along the spatial direction on each detector in each echelle order[2] have been taken into account in the normalization of the emission line fluxes $F(\lambda)$ with respect to the Hβ flux $F(\mathrm{H}\beta)$. We observed Lin49 and the flux standard star GD153 (Bohlin, Colina & Finley 1995) in the two different locations on the slit with a position angle of 219°, i.e. using an AB sequence in series of 120 s exposures and an ABBA sequence in exposures of 600 s (the separation between A and B positions is 5 arcsec). In Fig. 1, we show the slit positions on the z'-band (λ_c = 8897 Å) image taken by the acquisition and guiding camera.

We reduced the data using the echelle spectra reduction package ECHELLE and the two-dimensional spectra reduction package TWODSPEC in IRAF.[3] We subtracted the sky background and the bias current directly from the object frames. In the sequence, we subtracted the scattered light using the IRAF task APSCATTER. We used the intensity normalized instrumental flat frame to correct the sensitivity of each pixel in the residual frames and grating blaze function in each echelle order. We extracted the spectra between 3161 and 5904 Å in the UVB arm, 5578 and 10 255 Å in the VIS arm, and 9919 and 24 791 Å in the NIR arm. For the wavelength calibration of the UVB and VIS spectra, we used the Th-Ar comparison lines, and for the calibration of the NIR spectra, we used the OH lines recorded in the object frames in addition to Hg/Ar/Ne/Xe comparison lines. The resulting resolving power ($\lambda/\Delta\lambda$) is 8663–9650 in the UVB arm, 8409–8473 in the VIS arm, and 4289–5417 in the NIR arm, measured from the full width at half-maxima (FWHMs) of over 400 comparison lines in each arm. After we corrected the count rates for airmass and median combined the frames of Lin49 and GD153, we performed flux calibration and telluric corrections. The resulting XSHOOTER spectrum is displayed in Fig. 2.

[1] The slit width is 1.0 arcsec in the UVB and 0.9 arcsec in the VIS and NIR arms, respectively. The Hβ 4861 Å line is detected in the UVB arm.
[2] These were measured directly from the observed spectra: 0.16–0.17, 0.15–0.17, and 0.24–0.26 arcsec in the UVB, VIS, and NIR arms, respectively.
[3] IRAF is distributed by the National Optical Astronomy Observatories, operated by the Association of Universities for Research in Astronomy (AURA), Inc., under a cooperative agreement with the National Science Foundation.

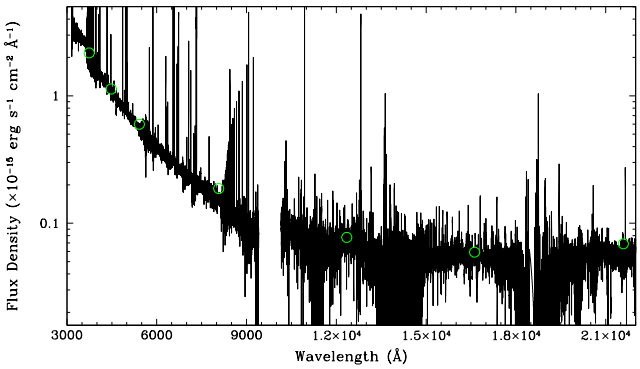

Figure 2. The XSHOOTER spectrum of Lin49. The flux density was scaled to the *V*-band magnitude $m_V = 17.225$ from the Magellanic Clouds Photometric Survey (MCPS; Zaritsky et al. 2002) in the UVB and VIS spectra and the Two Micron All Sky Survey (2MASS; Skrutskie et al. 2006) *J*-band magnitude $m_J = 16.58 \pm 0.08$ (Sloan et al. 2014) in the NIR spectrum. The green circles are these photometry results. Interstellar extinction was corrected for both the XSHOOTER spectrum and the photometry.

The resulting signal-to-noise (S/N) ratios measured in the continuum of the resultant spectrum are $\gtrsim$10. Fringes appear in the UVB spectrum with amplitudes ∼4–6 per cent of the local continuum intensity. These fringes pose a problem in determining the baseline of the continuum and subsequent equivalent width measurements and line-profile fittings in the stellar absorption analysis. Therefore, in order to minimize the fringing effect, we derived a smoothed spectrum using 9 pixel medians. As a result, the fringe amplitude decreased to ∼2 per cent and the spectral resolution decreased to ∼1/3 of the original value. We used this smoothed spectrum in the stellar absorption analysis.

2.2 *Spitzer*/IRS spectroscopy

We analysed the archival mid-IR *Spitzer*/IRS spectra taken with the SL (5.2–14.5 μm) and the LL modules (13.9–39.9 μm). The data were originally taken by Sloan (Programme ID: 50240, AOR Key: 27537664) on 2008 August 4 and presented in Sloan et al. (2014). We processed them using the data reduction packages SMART v.8.2.9 (Higdon et al. 2004) and IRSCLEAN v.2.1.1, provided by the *Spitzer* Science Center. Since the flux density of the *Spitzer*/MIPS (Multiband Imaging Photometer for Spitzer; Rieke et al. 2004) spectrum at the band 24 μm ($\lambda_{\rm centre}$ = 23.84 μm) is 9.77(−14) ± 3.90(−15) erg s^{-1} cm^{-2} μm^{-1} [4] (Sloan et al. 2014), and this value is consistent with the corresponding band flux density in the *Spitzer*/IRS spectrum, we do not perform flux density correction.

In Fig. 3, we present the resulting spectrum (red line) along with the spectrum of Tc1 (black line). The spectral resolution of the Tc1 data taken by the short-high and long-high resolution modules was reduced to match that of Lin49's. We did not remove atomic gas lines from the Tc1 spectrum, so the C_{60} 18.9 μm and [S III] 18.7 μm line complex in Tc1 is shifted towards the blue relative to the same complex in Lin49.

Lin49 and Tc1 show a broad 6–9 μm band, and broad 11 and 30 μm bands. The 17.4 and 18.9 μm C_{60} resonances are very strong with respect to the local continuum. The band profiles and strengths of these C_{60} features in both PNe are very similar. The 6–9 μm profiles in Lin49 and Tc1 are similar to the 6–9 μm thermal emission

[4] Here and henceforth we use the notation 9.77(−14) to mean 9.77 × 10^{-14}.

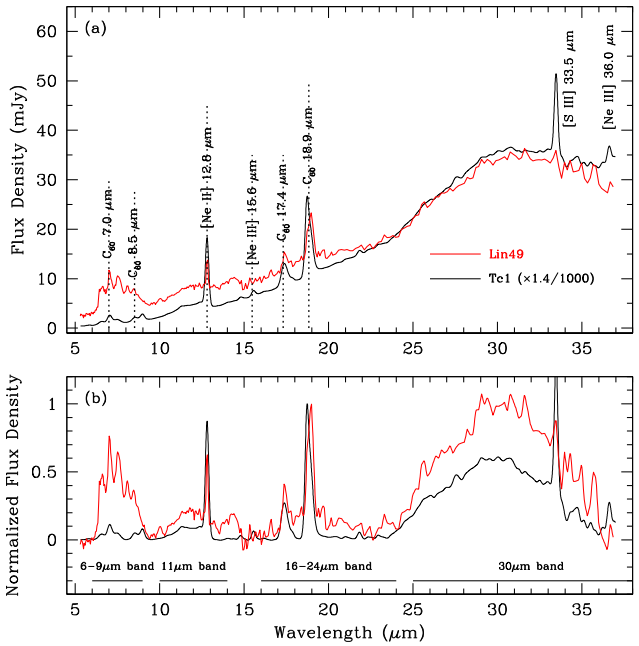

Figure 3. (a) *Spitzer*/IRS spectra of Lin49 and Tc1. The spectral resolution of the Tc1 spectrum was reduced to match that of the Lin49 spectrum. The positions of prominent atomic gas emission lines as well as C_{60} bands are indicated. (b) Comparison between the intensity normalized spectra of Lin49 and Tc1. We subtracted the local continuum by spline fitting in order to highlight the emission from dust grains and molecules, and then we normalized the resulting spectra to the peak flux density of the C_{60} 18.9 μm band.

from hydrogenated amorphous carbon (HAC) as displayed in Scott, Duley & Jahani (1997b). HAC is a generic name for a mixture of aliphatic and aromatic carbon, consisting of polycyclic aromatic hydrocarbon (PAH) clusters embedded within a matrix of aliphatically bonded material.

The differences between Lin49 and Tc1 are the degree of excitation of the nebula (the [Ne III] 15.55/36.01 μm lines are too weak to be clearly seen in Lin49, suggesting that the excitation degree of the Lin49's nebula is significantly lower than that of Tc1; indeed, we could not detect the [Ne III] nebular lines in the XSHOOTER spectrum) and the broad 16–24 μm band. As far as we know, the broad 16–24 μm feature has been seen in C-rich PNe and it is not limited to fullerene-containing C-rich PNe. Although the nature of this feature has been discussed by Bernard-Salas et al. (2009), García-Hernández et al. (2012), Otsuka et al. (2013), and Otsuka (2015), the carrier is still under debate.

3 RESULTS

3.1 Nebular line analysis

3.1.1 Flux measurements and interstellar extinction

We identified 186 atomic emission lines in the XSHOOTER and *Spitzer*/IRS data of Lin49. From Gaussian fits, we obtained central wavelengths and fluxes for these emission lines. De-reddened line fluxes $I(\lambda)$ were calculated using the following formula:

$$I(\lambda) = F(\lambda) \cdot 10^{c(\mathrm{H}\beta)(1+f(\lambda))}, \quad (1)$$

where $F(\lambda)$ is the observed flux, $c(\mathrm{H}\beta)$ is the reddening coefficient normalized by Hβ, and $f(\lambda)$ is the interstellar extinction function at

Table 1. The calculated $c(\mathrm{H}\beta)$. We used $c(\mathrm{H}\beta)$ for each spectral band. By adopting the $f(\lambda)$ of Cardelli, Clayton & Mathis (1989) with $R_V = 3.1$ and the average $c(\mathrm{H}\beta)$, we derived $E(B-V) = 0.07 \pm 0.01$ towards Lin49 (including the extinction in the MW) using the relation: $c(\mathrm{H}\beta) = 1.45E(B-V)$.

Band	$c(\mathrm{H}\beta)$	Using lines
XSHOOTER-UVB	0.10 ± 0.04	Hγ
XSHOOTER-VIS	0.12 ± 0.02	Hα
XSHOOTER-NIR-*J*	0.10 ± 0.01	Paγ, Paβ
XSHOOTER-NIR-*H*	0.10 ± 0.02	Br10
XSHOOTER-NIR-*K*	0.11 ± 0.02	Brγ
Average	0.11 ± 0.01	

λ computed from the reddening law. Several extinction functions for the MW and the Magellanic Clouds (MCs) are available (e.g. Savage & Mathis 1979; Seaton 1979; Howarth 1983; Prevot et al. 1984; Fitzpatrick 1986; Cardelli et al. 1989), with no significant difference in the value for XSHOOTER wavelengths. In the present work, we adopted the $f(\lambda)$ from Cardelli et al. (1989) with $R_V = 3.1$.

We derived $c(\mathrm{H}\beta)$ from the comparison of the observed ratios of Hγ, Hα, Paγ, Paβ, Br10 1.736 μm, and Brγ to Hβ with the corresponding theoretical ratios given by Storey & Hummer (1995) for an electron temperature $T_e = 10^4$ K and electron density $n_e = 10^4$ cm^{-3}, under the Case B assumption. We list the calculated $c(\mathrm{H}\beta)$ values and their 1σ uncertainty in Table 1. For each spectral band, we adopt its corresponding value of $c(\mathrm{H}\beta)$ to perform the extinction correction. The fluxes of the detected lines in Table B1 are normalized to $I(\mathrm{H}\beta) = 100$.

3.1.2 *Flux normalization of* Spitzer*/IRS and the Hβ flux of the whole PN*

Ideally, one would use the hydrogen fluxes given by the *Spitzer*/IRS observations to normalize the [Ne II] 12.81 μm flux (F([Ne II] 12.81 μm) $= (1.45 \pm 0.05) \times 10^{-14}$ erg s^{-1} cm^{-2}). This is preferred because there would be no need to correct for the interstellar reddening and for the difference in aperture sizes. However, we were not able to isolate the H I 7.46/11.31/12.37 μm lines to measure their fluxes, as these are weak lines in the spectrum of Lin49 and are potentially contaminated by the C_{60} 7.0 μm and [Ar II] 6.99 μm lines, and might be blended with the 7.7/11.3/12.3 μm PAH features. Therefore, we estimate $F(\mathrm{H}\beta)$ of the whole PN to be $1.02(-13) \pm 2.15(-15)$ erg s^{-1} cm^{-2} using the V-band magnitude ($m_V = 17.225 \pm 0.026$; Zaritsky et al. 2002) and scale it to the flux density of the XSHOOTER UVB spectrum to match this band magnitude.

The $c(\mathrm{H}\beta)$ value in the last line of Table 1 is the average value amongst the calculated $c(\mathrm{H}\beta)$ values. Using the average $c(\mathrm{H}\beta)$, we derived the de-reddened Hβ flux, $I(\mathrm{H}\beta)$, in the whole nebula to be $1.30(-13) \pm 4.88(-15)$ erg s^{-1} cm^{-2}. Thus, we obtained the I([Ne II] 12.81 μm) $= 11.169 \pm 0.551$, where $I(\mathrm{H}\beta) = 100$.

3.1.3 *Electron density and temperature*

In the following nebular line-diagnostics and subsequent ionic abundance calculations, the adopted transition probabilities, effective collision strengths, and recombination coefficients are the same as those listed in tables 7 and 11 of Otsuka et al. (2010).

With recombination lines (RLs), we calculated the T_e and n_e required for the He^+ and C^{2+} abundance derivations first. Following Zhang et al. (2005), we calculated the T_e(He I) using the He I I(7281 Å)/I(5876 Å) and I(7281 Å)/I(6678 Å) ratios and the emissivities of these He I lines given by Benjamin, Skillman & Smits (1999) for the case of $n_e = 10^4$ cm^{-3}. These three He I lines are insensitive to n_e when compared to the other He I lines. We adopted the average between the two T_e(He I) results (11 360 ± 840 K) to derive the number density ratio of the He^+ to the H^+ $n(He^+)/n(H^+)$. We did not detect any He II nebular emission lines in the XSHOOTER spectrum, so $n(He^{2+})/n(H^+) = 0$.

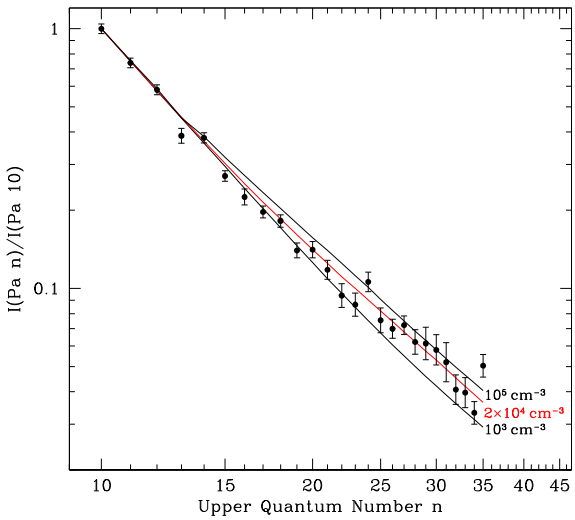

Figure 4. Intensity ratio of Paschen lines to Pa10, assuming Case B recombination. The theoretical intensity ratios (thick lines) are given for T_e = 9260 K determined from the Paschen jump and $n_e = 10^3$, 2×10^4, and 10^5 cm^{-3}.

The electron temperature derived from the Paschen jump T_e(PJ) by using equation 7 of Fang & Liu (2011).

In the last RL plasma diagnostics, we estimated n_e from the Paschen decrement. The intensity ratios of the high-order hydrogen lines to a lower order hydrogen line are sensitive to n_e, in particular when $n_e > 10^5$ cm^{-3}. We investigated such higher density regions using the Paschen series Pa n (n: principal quantum number of the upper level), as presented in Fig. 4. We compared the observed ratios of I(Pa n)/I(Pa 10) to the theoretical values in a range from 10^3 to 10^5 and T_e(PJ) = 9260 K in the Case B assumption, as computed by Storey & Hummer (1995). In Fig. 4, we plot the theoretical values in the cases of $n_e = 10^3$, 2×10^4, and 10^5 cm^{-3} with the observed ones. The 2×10^4 cm^{-3} model gives the best fit to the observed data (indicated by the red line, reduced χ^2 value is 0.95).

We derived n_e and T_e from collisionally excited lines (CELs) by solving the statistical equilibrium equation for the level populations using a multi-level atomic model. The values for n_e and T_e calculated from the diagnostic CEL ratios and the results obtained from the RL plasma diagnostics are listed in Table 2. The second, third, and last columns give the diagnostic lines, their line ratios, and the resulting values for n_e and T_e, respectively. The numbers in the first column indicate the ID of each curve in the n_e–T_e diagram in Fig. 5. Using this diagram, we determined the optimal n_e and T_e pairs.

Given that from the RL plasma diagnostics we know that in Lin49 T_e is around 10^4 K, we assume this as a constant value to calculate all n_e(CEL)s. Moreover, we assume a value of 6830 ± 1520 cm^{-3} for n_e([O II]) to derive T_e([N II],[O II],[S III],[O III]), and a value of 8910 ± 1460 cm^{-3} for n_e([S II]) to derive T_e([S II],[N I]). Since the [N I] 5200 Å line is partially affected by fringes, its flux and the n_e([N I]) are very uncertain. Therefore, we used n_e([S II]) to calculate T_e([N I]), instead of n_e([N I]). Note that the T_e([N I]) is also uncertain.

Table 2. Summary of plasma diagnostics using nebular lines.

ID	n_e diagnostic	Value	Result (cm^{-3})
(1)	[N I] (5198 Å)/(5200 Å)	2.179 ± 0.573	4890_{-3460}
(2)	[O II] (3726 Å)/(3729 Å)	2.200 ± 0.126	6830 ± 1520
(3)	[S II] (6716 Å)/(6731 Å)	0.507 ± 0.012	8910 ± 1460
	Paschen decrement		$\sim$20 000
ID	T_e diagnostic	Value	Result (K)
(4)	[N II] (6548 Å+6583 Å)/(5755 Å)	53.89 ± 2.15	$11\,660 \pm 230$
(5)	[O III] (4959 Å+5007 Å)/(4363 Å)	147.1 ± 12.7	$11\,090 \pm 320$
(6)	[S III] (9069 Å)/(6312 Å)	8.757 ± 0.419	$10\,300 \pm 220$
(7)	[N I] (5198 Å/5200 Å)/(1.04 μm)	3.706 ± 1.184	8960 ± 1650
(8)	[O II] (3726/29 Å)/(7320/30 Å)	9.523 ± 0.274	$10\,060 \pm 180$
(9)	[S II] (6717/31 Å)/(4069/76 Å + 1.029/1.034/1.037 μm)	1.702 ± 0.062	9050 ± 310
	He I (7281 Å)/(5876 Å)	0.061 ± 0.003	$11\,180 \pm 770$
	He I (7281 Å)/(6678 Å)	0.251 ± 0.012	$11\,540 \pm 620$
	(Paschen jump)/(Pa11)	0.102 ± 0.012	9260 ± 770

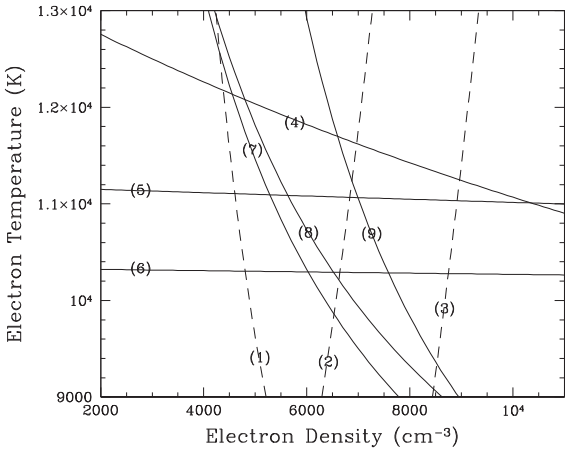

Figure 5. n_e–T_e diagram based on diagnostic CELs. The thick and dashed lines with the ID numbers (see Table 2) are the indicators of T_e and n_e, respectively.

Using equation 2 from Liu et al. (2000), we calculated the recombination contamination to the [O II] 7320/30 Å lines due to O^{2+} assuming $T_e = 10^4$ K, and find that it is very small (0.02 per cent of their observed de-reddened fluxes). In the T_e([O III]) and T_e([N II]) derivations, we do not subtract the recombination contribution of the O^{3+} and N^{2+} from the observed [O III] 4363 Å and [N II] 5755 Å fluxes, because we do not detect any O^{3+} and N^{2+} lines in the present spectra. As the $O^{2+}/(O^{+} + O^{2+})$ ratio is small ($\sim$0.03, see the next section), the O^{3+} and N^{2+} recombination contamination to [O III] 4363 Å (and perhaps [N II] 5755 Å, too) is probably very small.

We derived the electron densities in the neutral to low-ionization regions using the [N I], [S II], and [O II] nebular line ratios, whereas the electron density in higher ionization regions (e.g. derived from the [Ar IV] I(4711 Å)/I(4740 Å) ratio) cannot be calculated because Lin49 is a very low excitation PN, indicated by the I([O III] 5007 Å)/I(Hβ) = 0.16. However, we confirm that T_e([O III]) and T_e([S III]), and the volume emissivities of O^{2+}, Ne^{+}, S^{2+}, Cl^{2+}, and Ar^{2+} [these emissivities are calculated under the T_e([O III]) for O^{2+} and T_e([S III]) for the other ions and a constant n_e([O II])] do not change significantly when compared to those under an n_e(Paschen decrement) = 2×10^4 cm^{-3} ($\lesssim$3 per cent). This is neither the case for the ionic abundances.

3.1.4 *Nebular abundance derivations using ICFs*

We list the T_e and n_e pair adopted in each ionic abundance calculation in Table B2. The choices of T_e and n_e were driven by the ionization potentials of the target ions. We adopt a constant n_e = 10^4 cm^{-3} to calculate He^{+}/H^{+} using recombination coefficients of Benjamin et al. (1999) and C^{2+}/H^{+} using those of Davey, Storey & Kisielius (2000, the RL ionic abundances are not sensitive to n_e with $< 10^8$ cm^{-3}). The He^{+} and C^{2+} abundances were derived under the Case B assumption for the lines with levels that have the same spin as the ground state, and under the Case A assumption for lines of other multiplicities.

The results are summarized in Table B3, where the fifth and tenth columns show the number density ratio of the ion X^{m+} relative to H^{+} derived from the emission line with wavelength listed in the third and eighth columns. The adopted values calculated using a weighted average are listed in the last line for each ion (in boldface). In the two consecutive lines below the results for each ion, the ionization correction factor (ICF) and the elemental abundance are given.

The ICFs have been empirically determined based on the fraction of observed ion number densities with similar ionization potentials to the target element, and have also been theoretically determined based on the fractions of the ions calculated by photoionization (P-I) models. For Lin49, we tested the ICFs calculated by the P-I model of the C_{60} PN M1-11 performed by Otsuka et al. (2013), as well as the empirically determined ICFs. M1-11 is a Galactic C_{60} PN with a central star with similar T_{eff} to our target (31 830 K, while the central star of Lin49 has T_{eff} = 30 500 K – see the next section). The model of Otsuka et al. (2013) includes amorphous carbon and silicon carbide (SiC) grains and PAH molecules and aims to fit the observed UV to far-IR SED and match observed gas emission line fluxes. The interaction between gas and dust affects the thermal structure of the nebula. As a result, the ionization structure will be affected. Lin49 and M1-11 have similar T_{eff} of the central star as the heating/ionization source and similar C-rich dust features. Therefore, we assume that the ICFs calculated in the P-I model of M1-11 are reasonable values for Lin49. By adopting these ICFs, we also have the opportunity to test their robustness in the P-I modelling as discussed later.

The resulting elemental abundances $\epsilon(X)$ are listed in Table 3. These results are given in the form of $\log_{10}(X/H)+12$. The fourth column is the relative abundance to the solar abundance, taken from Lodders (2010). Except for Cl, there is no significant difference in the solar photospheric abundances between Lodders (2010) and Asplund et al. (2009). Although the results for Cl abundances in these two papers are in agreement within the uncertainties (5.26 ± 0.06 and 5.50 ± 0.30, respectively), those are still large uncertainties when compared to other elements and one should be careful when discussing the [Cl/H] results. This is also the case for the solar O abundance (the measurement uncertainties are very small but the solar O abundance seems to remain under debate; see, e.g., Asplund et al. 2009).

Below we give a detailed explanation for the C abundance. The calculation methods of the He, N, Ne, Cl, Ar, and Fe abundances are explained in Appendix A. The O and S abundance calculations are explained in the course of the He calculation.

Table 3. Elemental abundances based on the ICFs, solar abundances, relative abundances to the solar values, and the predicted elemental abundances in the AGB nucleosynthesis models by Fishlock et al. (2014) for initially 1.0, 1.25, and 1.5 $M_\odot$ stars with $Z = 0.001$. The C(RL) is the C abundance derived from the C^{2+} abundance using the recombination C II 4267 Å line and the C(CEL) is an *expected* value when we adopted the average CEL C/O ratio amongst six SMC C_{60} PNe. See the text for details.

X (1)	$\epsilon(X)$ (2)	$\epsilon(X_\odot)$ (3)	[X/H] (4)	$\epsilon(X_{model})$ for 1.0 $M_\odot$ (5)	$\epsilon(X_{model})$ for 1.25 $M_\odot$ (6)	$\epsilon(X_{model})$ for 1.5 $M_\odot$ (7)
He	10.80 to 11.01	10.93 ± 0.01	-0.13 to $+0.08$	10.99	11.01	11.01
C(RL)	8.67 ± 0.09	8.39 ± 0.04	$+0.28 \pm 0.10$	8.06	8.56	8.89
C(CEL)	8.46 ± 0.24	8.39 ± 0.04	$+0.07 \pm 0.25$	8.06	8.56	8.89
N	6.93 ± 0.02	7.86 ± 0.12	-0.93 ± 0.12	7.15	7.26	7.18
O	8.11 ± 0.01	8.73 ± 0.07	-0.62 ± 0.07	7.58	7.68	7.79
Ne	7.18 ± 0.05	8.05 ± 0.10	-0.89 ± 0.11	6.89	7.37	7.72
S	6.02 ± 0.01	7.16 ± 0.02	-1.15 ± 0.02	5.99	6.00	6.00
Cl	4.03 ± 0.05	5.25 ± 0.06	-1.22 ± 0.08	4.07	4.08	4.10
Ar	5.48 ± 0.11	6.50 ± 0.10	-1.02 ± 0.15	5.27	5.28	5.28
Fe	4.55 ± 0.04	7.46 ± 0.08	-2.91 ± 0.09	6.37	6.38	6.38

3.1.5 C abundance from RLs

Several prior studies on SMC PN abundances have reported the detection of RL carbon lines (e.g. Tsamis et al. 2003, 2004; Leisy & Dennefeld 2006; Shaw et al. 2010). As far as we know, the RL C^{2+} and C abundance derivations in Lin49 are only the second derivation for an SMC PN.

In Lin49, we need to take care when determining the C^{2+} abundance. The C^{2+}/H^+ determined from C II 3918.98/20.69 Å ($3p^2P$-$4s^2S$) is much higher than those obtained from other detected lines. This is due to intensity enhancement by resonant absorption of C II 635.25/636.99 Å ($2p^2P^o$-$4s^2S$) and then fluorescence by decay of the $4s^2S$ level. C II 7231.32/36.42 Å ($3p^2P$-$3d^2D$) may also be enhanced by such a resonance and fluorescence of C II 687 Å ($2p^2P^o$-$3d^2D$) and the $3d^2D$ decay. The $2p^2P^o$ level of the C II 6578.05 Å ($2p^2P^o$-$2s^2S$) could be affected by the C II 3918.98/20.69 and 7231.32/36.42 Å. Thus, C^{2+} abundances except for the value derived from C II 4267 Å ($3d^2D$-$4f^2F$) would be overestimated. Following a detailed report on fluorescence and RLs in the PN IC418 by Escalante, Morisset & Georgiev (2012), we supposed the C^{2+}/H^+ obtained from C II 4267 Å to be the most reliable, as this line has no paths directly connected to the $2p^2P^o$ level. We should note that C II line fluorescence enhancement is not common in low-excitation PNe. For example, Otsuka et al. (2013) and Otsuka, Hyung & Tajitsu (2015) do not observe such enhancements in M1-11 or in the C-rich PN K648 ($T_{\rm eff} = 36\,360$ K).

As discussed below, we test three different ICFs to derive the C abundance. The equation proposed by Kingsburgh & Barlow (1994)

$$\mathrm{C} = \mathrm{ICF(C)} \cdot \frac{\mathrm{C}^{2+}}{\mathrm{H}^+},$$
$$\mathrm{ICF(C)} = \frac{\mathrm{O}}{\mathrm{O}^{2+}} \qquad (2)$$

gives a value of ICF(C) = 32.2 ± 2.2 and ϵ(C) = 9.5 ± 0.09. Delgado-Inglada, Morisset & Stasińska (2014) calculated the C/O ratio in PNe from a P-I grid modelling, obtaining the following equation to derive the C abundance:

$$\mathrm{C} = \mathrm{ICF(C)} \cdot \frac{\mathrm{C}^{2+}}{\mathrm{H}^+},$$
$$\mathrm{ICF(C)} = \frac{\mathrm{O}}{\mathrm{O}^{2+}} \cdot \left(0.05 + 2.21\omega - 2.77\omega^2 + 1.74\omega^3\right),$$
$$\omega = \frac{\mathrm{O}^{2+}}{\mathrm{O}^+ + \mathrm{O}^{2+}}. \qquad (3)$$

Note that equation (3) is valid in the range $0.05 < \omega < 0.97$ and, therefore, is not valid for Lin49, for which ω is 0.031 ± 0.002. Nevertheless, we applied equation (3) to our data, and obtained ICF(C) = 37.8 ± 3.4 and ϵ(C) = 9.65 ± 0.09. The uncertainty in the C/O ratio (i.e. the C abundance) is higher near the lower limit of the valid ω interval. Delgado-Inglada & Rodríguez (2014) estimated a confidence interval from −1 to +0.26 dex in the low-excitation PN NGC 40, which has an ω (0.03) very similar to Lin49. In low-ionization PNe such as NGC 40 and Lin49, the same applies for the ICF(C) given by Kingsburgh & Barlow (1994). Thus, equations (2) and (3) are not ideal to determine ϵ(C) in Lin49, and the result would lie in the wide range from 8.6 to 10, taking into account the confidence limit of −1 to +0.26 dex. This might be due to the reason that the respective fractions of the C^{2+} and O^{2+} relative to C and O are very different in low-excitation PNe. As the models from Delgado-Inglada et al. (2014) do not target low-excitation PNe alone, their ICF(C) does not reproduce the C/O ratio properly using the C^{2+} and O^{2+} abundances.

For the above reasons, we adopt the ICF(C) and the ϵ(C) derivations based on the P-I model of M1-11, as given by the following equations:

$$\mathrm{C} = \mathrm{ICF(C)} \cdot \frac{\mathrm{C}^{2+}}{\mathrm{H}^+},$$
$$\mathrm{ICF(C)} = 2.46 \cdot \frac{\mathrm{S}}{\mathrm{S}^{2+}}. \qquad (4)$$

We chose to write the ICF(C) as a function of the S and S^{2+} abundances (instead of writing it as a function of O abundances), as the ionization potential of C^{2+} is similar to that of S^{2+}. The C^{2+} fraction was 0.338 in the P-I model of M1-11. From equation (4), we get ICF(C) = 3.96 ± 0.23 and the RL ϵ(C) = 8.67 ± 0.09.

3.1.6 Expected C abundance from CELs

In the field of PN research, it is well known that the C, N, O, and Ne abundances derived from RLs are larger than those derived from CELs. Several explanations for the abundance discrepancies have been proposed, and consensus has yet to be reached, see e.g. Liu (2006) for the historical background and the abundance discrepancy problem. We believe that the C abundance derived from the C II 4267 Å line would be reasonable and acceptable as the C abundance for an SMC PN. Otsuka et al. (2010) argued that the emissivities of the C III] 1906/09 Å lines are very sensitive to T_e because of the energy difference of these lines between upper and lower level,

Table 4. Effective temperature of the central star ($T_{\rm eff}$), nebular radius (r), and nebular elemental abundances in SMC C_{60} PNe. ϵ(C) are derived from C CELs. ϵ(C) in SMC1 was estimated using the O abundances of Leisy & Dennefeld (2006) and the C/O ratios of Vassiliadis et al. (1998). The ϵ(C) in Lin49 is an *expected* value when we adopted the average CEL C/O ratio amongst the other SMC C_{60} PNe. We excluded the ϵ(C) of Lin49 to calculate the average ϵ(C) amongst these PNe.

C_{60} PNe	$T_{\rm eff}$ (K)	r (arcsec)	ϵ(He)	ϵ(C)	ϵ(N)	ϵ(O)	ϵ(Ne)	ϵ(S)	ϵ(Ar)	References
SMC1	37 000	0.15	10.83	8.00	7.16	7.86	6.42	<6.94	5.71	(1),(2),(3),(4),(10)
SMC13	31 300	0.19	11.11	8.73	7.30	8.06	7.35	5.96	5.46	(4),(5),(6),(7)
SMC15	58 000	0.17	11.03	8.26	7.71	8.07	7.32	7.67	5.72	(1),(6),(8),(9)
SMC16	37 000	0.18	10.69	8.19	6.55	7.85	6.37	6.39	5.46	(1),(6),(8),(9)
SMC18	31 500	0.15	11.06	8.31	7.11	7.90	7.57	6.18	5.67	(4),(5),(6),(7)
SMC24	37 800	0.20	11.13	8.18	7.17	8.06	7.36	6.11	5.58	(4),(5),(6),(7)
Average	38 770	0.17	10.98	8.28	7.17	7.97	7.07	6.54	5.64	
Lin49	30 500	0.23	10.8–11.01	8.46	6.93	8.11	7.18	6.02	5.48	(10)

References – (1) Leisy & Dennefeld (2006) for abundances; (2) Vassiliadis et al. (1998) for the C/O ratios of 1.38 in SMC1; (3) Herald & Bianchi (2007) for $T_{\rm eff}$; (4) Stanghellini et al. (2003) for r; (5) Shaw et al. (2010) for abundances except ϵ(C); (6) Stanghellini et al. (2009) for ϵ(C); (7) Villaver, Stanghellini & Shaw (2004) for $T_{\rm eff}$; (8) Shaw et al. (2006) for r; (9) Dopita & Meatheringham (1991a) for $T_{\rm eff}$; (10) This work.

$\Delta E = k\,\Delta T$ (k: the Boltzmann constant), where $\Delta T = 75\,380$ K and the C^{2+} abundances from RLs may be more reliable than those from CELs if one cannot find representative $T_{\rm e}$ values in the CEL C^{2+} emitting zone. However, it is unclear whether our measured RL C abundance is representative for Lin49; the RL abundances might represent those in high-density zones, hydrogen-deficient cold components, or stellar wind whereas the CEL abundances might indicate the average in the nebula (see Otsuka et al. 2010, and references therein).

For the above reasons, we estimate the CEL C abundance in Lin49 as follows. In the measurement of the CEL C abundances for extended objects, the flux normalization issue would be raised due to the different sizes and shapes of the slits used in UV (to obtain the UV C III] 1906/09 Å and [C II] 2320-30 Å lines) and optical spectroscopy (to obtain e.g. Balmer lines) and the different slit positions putting on the targets. As a consequence, the measured CEL C abundances may be largely inconsistent with the RL C values, whereas in objects compact enough for the slit dimension, such as MC PNe, the flux normalization issue can be avoided. Using the *Hubble Space Telescope*/Faint Object Spectrograph and the Space Telescope Imaging Spectrograph, the CEL C abundances have been measured in the SMC C_{60} PNe SMC1, 13, 15, 16, 18, and 24. In Table 4, the abundances of these PNe, the nebula radii, and the effective temperatures are compiled, with the last line the average value of each parameter. The O abundances in this table are measured from O CELs. The average C/O abundance ratio is 2.28 (with a standard deviation of 1.27) amongst these six PNe. Supposing that these six PNe and Lin49 evolved from stars with similar initial masses (because the elemental abundances of all these PNe are very similar) and that their current evolutionary stage is also similar [because both the effective temperature of the central star and the radius of the nebula are consistent with similar ages after the asymptotic giant branch (AGB) phase], we estimate the CEL C abundance for Lin49 to be $(2.91 \pm 1.63)\times10^{-4}$, or CEL ϵ(C) = 8.46 ± 0.24 using this C/O ratio and the observed O abundance. Hereafter, we regard this CEL ϵ(C) as a representative C abundance in Lin49 and used this value in subsequent SED modelling.

3.1.7 Metallicity

In comparison to α-elements S and Ar, Fe (a refractory element) is highly depleted. The extremely low [Fe/H] abundance indicates that most iron atoms are trapped in dust grains. As a consequence, the Fe nebular abundance does not reflect the metallicity of Lin49.

For the purpose of this study, we wonder how much Fe is depleted on to dust grains, and correspondingly what is the true metallicity of Lin49. The SMC is an irregular galaxy formed through strong interactions between the LMC and the MW Galaxy. Mucciarelli (2014) reported that the typical metallicity of the old stellar populations in the SMC is ~-0.9 in [Fe/H]. Although the chemical evolution of the SMC would be incompatible with that of the MW, we attempt to estimate the metallicity of Lin49 using the chemical evolution model of the MW halo by e.g. Kobayashi, Karakas & Umeda (2011) taking current circumstance that the chemical evolution of the SMC based on the observed abundances remains unclear but a typical [Fe/H] in the SMC is close to a typical [Fe/H] in the MW halo. Kobayashi et al. (2011) reported that the [S/Fe] and [Ar/Fe] are $\sim+0.4$ and $\sim+0.3$ in the [Fe/H] < -1, respectively. By applying this prediction and from the [S/H] and [Ar/H] observed in Lin49, we obtain [Fe/H] $= -1.55$ and -1.32, respectively. By comparing the average [Fe/H] of $= -1.40$ with the observed [Fe/H] $= -2.91$, we conclude that 96 per cent of the iron atoms in the Lin49 nebula are trapped in dust grains. Although the value has large uncertainty, we estimate that the metallicity Z of Lin49 is $\sim$0.0006 or $\sim0.04\,Z_{\odot}$. Here, $Z_{\odot}$ is the solar metallicity. In the following discussion, we adopt $Z = 0.0006$ ($0.04\,Z_{\odot}$).

3.1.8 Comparison with the AGB nucleosynthesis model

In the last two columns of Table 3, we list the predicted abundances in the AGB nucleosynthesis models for 1.0, 1.25, and 1.50 $M_{\odot}$ main-sequence mass stars with $Z = 0.001$ by Fishlock et al. (2014). Our observed nebular abundances are in excellent agreement with these predictions except for O.

In the comparison between the model results and the observed abundances in LMC post-AGB stars, Fishlock et al. (2014) found that the model predicted [O/Fe] is overabundant relative to the observed values. They discussed the possibility that the initial O abundances in these post-AGB stars are greater than the scaled-solar initial abundance set in the model. The enhancement of the O abundance in Lin49 could not be explained by the extra $^{13}C(\alpha,n)O^{16}$ reaction in the He-rich shell; if that were the case, we should have observed more enhanced C, O, and n-capture element abundances. The O abundance in Lin49 could be not polluted by local events such as Type II supernovae (α-elements producers) and is not different from the nearby PNe. For instance, Lin45 [the nearest PN from Lin49; the linear distance projected on sky is 438 arcsec (or 131 pc at 61.9 kpc) from the position of Lin49] shows similar O and

α-elemental abundances (He = 10.93, N = 6.52, O = 8.20, Ne = 7.55, S = 6.28, Ar = 5.79; Costa, de Freitas Pacheco & Idiart 2000, the line-of-sight depths towards Lin49 and Lin45 are unknown, though). Therefore, we think that the initial O abundance in Lin49 is larger than we expected. This could be the case for the other C_{60} PNe listed in Table 4.

Although our abundance determinations depend on models of H II regions (for He) and M1-11 (for He, C, Ne, Cl, and Ar) and that there might be some issues with the C and O abundances, the 1.25 $M_\odot$ model fits to the Lin49 abundances better. From the view of elemental abundances, the initial mass of the progenitor in Lin49 and the other SMC C_{60} PNe would be around 1–1.25 $M_\odot$.

3.2 Characterizing the central star through the analysis of absorption lines

We produced a synthetic spectrum to fit the observed XSHOOTER spectrum after 9 pixel median smoothing in order to reduce the fringe amplitude (see section 2.1). With this model spectrum, we derived the photospheric abundances, $T_{\rm eff}$, and surface gravity (log g) of the central star. We used the O-type star grid model OSTAR2002 by Lanz & Hubeny (2003) using the non-local thermodynamic equilibrium (non-LTE) stellar atmosphere modelling code TLUSTY[5] (Hubeny 1988). The OSTAR2002 grid consists of 690 metal line-blanketed, non-LTE, plane-parallel, and hydrostatic model atmospheres. We fitted absorption lines of He, C, N, O, and Si as we identified absorption lines of these elements in the observed spectrum.

Based on the assumption that the metallicity of the central star is the same as that of the nebula, we adopt a metallicity $Z = 0.04\,Z_\odot$ as determined in Section 3.1.7. We set the instrumental line broadening determined by measuring Th-Ar comparison lines. In reference to the stellar absorption fitting report for the Galactic C_{60} PN IC418 by Morisset & Georgiev (2009), we set the microturbulent velocity to 5 km s^{-1} and the rotational velocity to 20 km s^{-1}; the synthesized spectra using SYNSPEC[6] with these values can fit the observed absorption line profile.

To determine $T_{\rm eff}$ and log g, we first run P-I models using CLOUDY with a stellar atmosphere by TLUSTY OSTAR2002 in order to find the ranges of $T_{\rm eff}$ and log g because we do not detect any $T_{\rm eff}$ diagnostic lines with a high S/N ratio. These models keep the photospheric abundances at He/H = 0.1 and the metallicity at 0.04 $Z_\odot$. In the CLOUDY models, our initial guess for $T_{\rm eff}$ is 32 000 K, as given by equation 3.1 of Dopita & Meatheringham (1991b), which was established from optically thick MC PNe. T_Z(H I) was 32 950 K by the Zanstra method. The initial guess for log g was determined by fitting to the profiles of the Hγ line (we blocked the portion of the nebular line in the fitting process), and He II 4686 Å line with He/H = 0.1. We obtain a range of log g between 3.2 and 3.4 cm s^{-2}. From these initial guesses for $T_{\rm eff}$ and log g, we run CLOUDY models to match the observed nebular emission line fluxes and abundances, and to further constrain the $T_{\rm eff}$ and log g ranges. Within these ranges, we perform profile fitting of the Hδ, Hγ, and He II lines again. Finally, we derive $T_{\rm eff}$ = 30 500 ± 500 K and log g = 3.29 ± 0.05 cm s^{-2}.

Adopting these values for $T_{\rm eff}$ and log g, we fit the He II 4686 Å line profile to determine the He abundance. Since the weak He II absorption lines were partially affected by fringes in the spectrum, the He/H abundance derived by the line fitting method presents a large uncertainty. Subsequently, we determined the C, N, O, and Si abundances to match the observed line profiles. The C abundance was obtained using the C IV 5801/5811 Å lines. The O abundance was derived using the O III 3755/3774/3791 Å lines, and the Si abundance was derived using the Si IV 4089/4116 Å lines. Finally, the N abundance was obtained by fitting the N III + O II 4097 Å line complex after we determined the O abundance. Some of the absorption lines, e.g. the C III 4152/4156/4163 Å and the O II 4189 Å, could not be fitted by the best model with log g = 3.29 cm s^{-2}. This might be because we could not determine $T_{\rm eff}$ and log g with considerable accuracy. However, if we set log $g \gtrsim 3.4$ cm s^{-2}, we were able to reproduce these C III lines as absorption lines. However, with such a high surface gravity, we cannot fit the line profiles of the He I,II and H I lines.

We display the synthesized stellar spectrum in the range between 3720 and 4910 Å in Fig. 6. In Table 5, we list the derived quantities with their 1σ uncertainties. With the exception of He, the stellar abundances are systematically larger than the nebular abundances by ∼0.6 dex; the stellar abundance could reflect the latest nucleosynthesis result. The stellar C/O ratio (2.57 ± 1.90) supports a C-rich classification for Lin49, and our adopted nebular C/O ratio (2.28) for the CEL C derivation could be appropriate.

3.3 Fitting the broad 30 μm feature

Otsuka et al. (2014) fitted the 13–160 μm SED of 11 Galactic C_{60} PNe using synthesized absorption efficiency ($Q_{\rm abs,\lambda}$) based on the spectral data set of IC418, and concluded that strength of the broad 30 μm feature with respect to the underlying continuum in these objects is constant. The carrier for this feature remains unclear and is under debate (e.g. see Otsuka et al. 2014, for details). We use the same approach to fit the broad 30 μm feature in Lin49 using $Q_{\rm abs,\lambda}$ from Otsuka et al. (2014). We utilized equations 2 and 3 of Otsuka et al. (2014) with $p = q = 2$ and a lower limit on the dust temperature of 20 K, as adopted in Otsuka et al. (2014). The model of Otsuka et al. (2014) assumes that the dust density, as a function of the distance from the central star of planetary nebula (CSPN) r, is distributed around the CSPN with a power law ($\propto r^{-p}$) and that the dust temperature distribution $T_{\rm d}(r)$ also follows a power law ($\propto r^{-q}$). As listed in Table 6, we performed two fits, Fit1 and Fit2, where the difference between them is the wavelength range over which the fit is performed. Fit1 (fitting region is 15–16 and 20–36 μm) is an entire fit for the broad 16–24 and 30 μm features to verify the conclusion of Otsuka et al. (2014). The resulting maximum dust temperatures ($T_{\rm d}$(max)) are listed in Table 6.

As presented in Fig. 7, the SED predicted by Fit1 (indicated by the red line) can explain the SED except for $\lambda \gtrsim 28$ μm where the model underestimates the observed flux density. At this moment, we have two explanations for this underestimation; one might be the high noise level in the data around the wavelength range 28–36 μm (a gap or a bump around 30 μm is seen). In fitting for the broad 30 μm feature, while the other could be the resulting effect of the contribution from other dust components to the 30 μm feature, e.g. iron-rich magnesium sulphides such as $Mg_{0.5}Fe_{0.5}S$[7] (Begemann et al. 1994), as Lin49 is an extremely Fe deficient ([Fe/H] = −2.91) PN. Although there are no reports of the detection of iron-rich magnesium sulphides or iron dust in IC418 and C_{60} PN M1-20, the nebular Fe abundances in these PNe are extremely depleted,

[5] See http://nova.astro.umd.edu

[6] See http://nova.astro.umd.edu/Synspec49/synspec.html

[7] http://www.astro.uni-jena.de/Laboratory/OCDB/sulfides.html

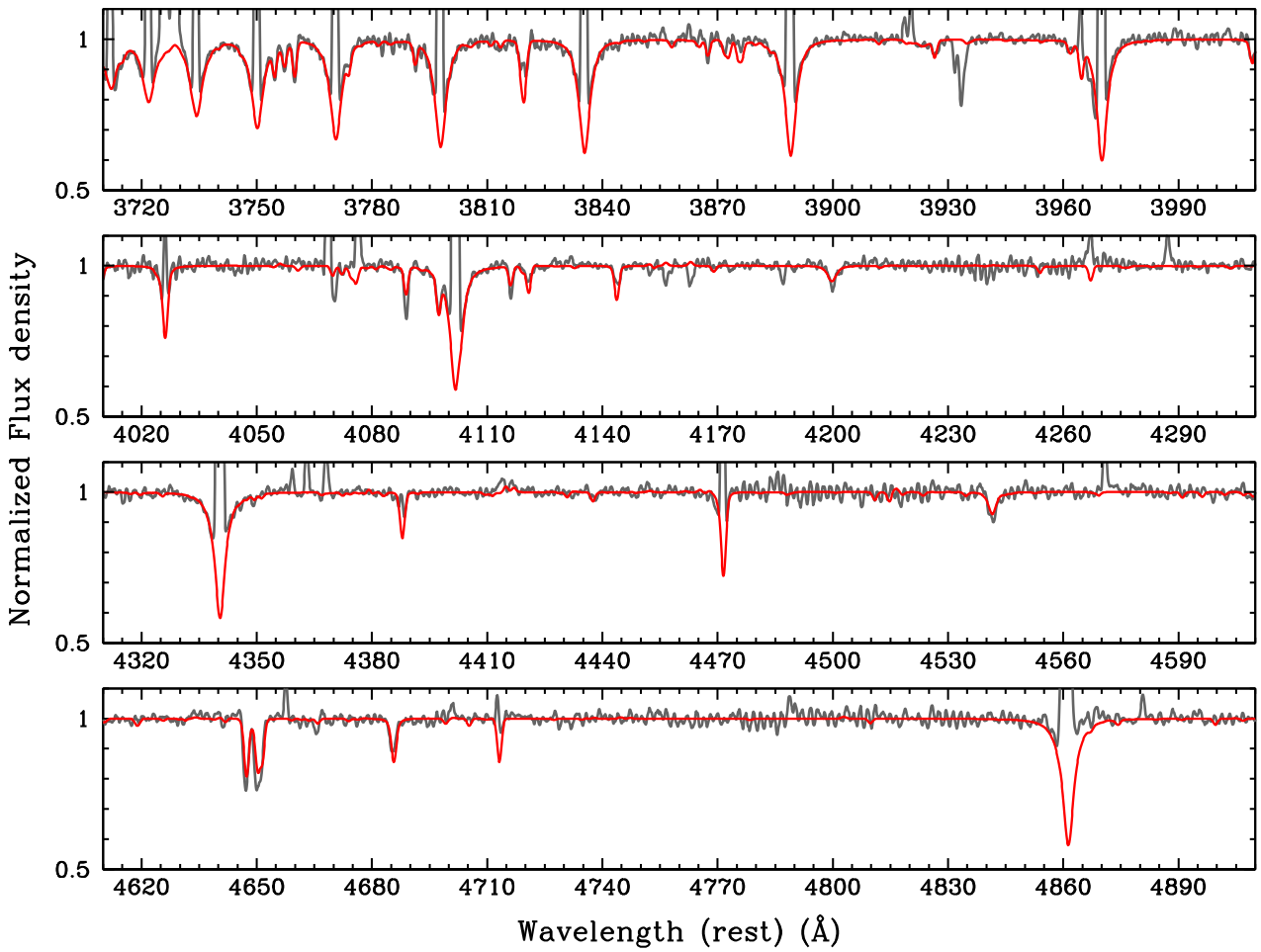

Figure 6. The synthesized spectrum of Lin49 in the range between 3720 and 4910 Å as given by our TLUSTY modelling (red line) and the observed XSHOOTER spectrum (grey line, after 9 pixel median smoothing). The FWHM of the synthesized spectrum was set to be constant and equal to 1.2 Å.

Table 5. The results of the TLUSTY modelling for the stellar spectrum.

Parameter	Derived value
$T_{\rm eff}$ (K)	30 500 ± 500
log g (cm s^{-2})	3.29 ± 0.06
ϵ(He)	10.88 ± 0.30
ϵ(C)	9.02 ± 0.30
ϵ(N)	7.60 ± 0.30
ϵ(O)	8.61 ± 0.10
ϵ(Si)	6.76 ± 0.30

Table 6. Fitting results for the broad 30 μm feature and the predicted flux densities at 65, 90, and 120 μm. The uncertainty of the predicted flux densities is ∼3 per cent.

Model	Fit range (μm)	$T_{\rm d}$(max) (K)	F_ν(65 μm) (mJy)	F_ν(90 μm) (mJy)	F_ν(120 μm) (mJy)
Fit1	15–16, 20–36	155.5 ± 1.4	5.90	3.38	1.80
Fit2	24–36	126.0 ± 1.4	8.93	5.56	3.13

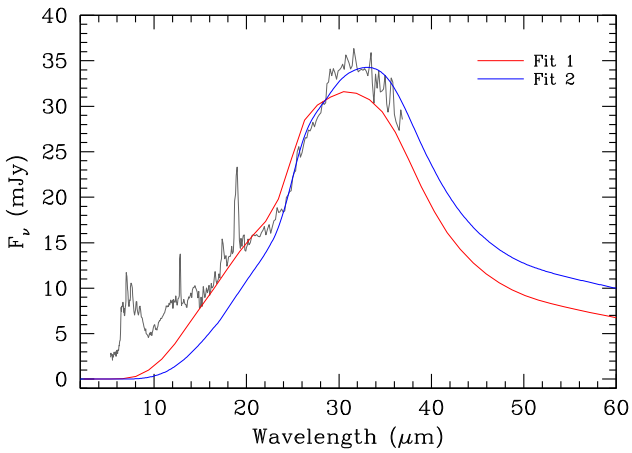

Figure 7. Fits of the broad 30 μm feature (indicated by the red and blue lines) overlaid on the *Spitzer*/IRS spectrum of Lin49 (grey line). Fits 1 and 2 are different in terms of the fitting wavelength range. The fitting results are summarized in Table 6.

according to the results of Delgado-Inglada & Rodríguez (2014), who reported that the respective nebular O and Fe abundances in IC418 are 8.52 and 4.36–4.56, corresponding to the [O/H] = −0.21 and [Fe/H] = −3.1 to −2.9 (see Delgado-Inglada & Rodríguez 2014, about the nebular O and Fe abundances in M1-20). In M1-11, Otsuka et al. (2013) reported the nebular [O/H] = −0.07 and [Fe/H] = −2.42. The Fe-depletion will differ from object to object. Therefore, the strength of the 30 μm feature with respect to local

dust continuum would be different in each PN if any iron-rich magnesium sulphides contribute to this feature. We will give a possible explanation of the extreme Fe-depletion in Lin49 later.

The Fit2 for the wavelength range 24–36 μm (the blue line in Fig. 7) is a complementary test for the same hypothesis. The predicted SED underestimates the 16–24 μm flux density. Taking into account the Fit1 result at this moment is difficult to completely agree with the conclusion of Otsuka et al. (2014) based on the current data quality.

We list the predicted flux densities at 65, 90, and 120 μm. Fit1 and Fit2 give a lower limit and an upper limit in these far-IR wavelengths. We use these average flux densities to constrain the SED fitting (see section 3.4).

3.4 P-I modelling

Using a modified code based on CLOUDY (Ferland et al. 1998, version C13.03), we fit the SED and investigate the physical conditions of the gas and dust grains in the nebula, and derive their masses (m_g and m_d, respectively). In this modified code, we substituted the transition probabilities and effective collision strengths of CELs by the same values used in our plasma diagnostics and nebular abundance determinations for consistency.

The effective collision strengths of several lines such as [Ar II] 6.99 μm in the original CLOUDY were constant values not functions of the T_e. The constant collision strengths of these ions could lead to the overprediction of line fluxes as reported in Otsuka et al. (2013), and could affect the P-I model results of the gas temperature and ion fraction of each element inside the nebula. For example, the predicted I([Ar II] 6.99 μm)/I(Hβ) was ∼3/100 when we adopted the effective collision strength of this line used in the original CLOUDY. After revising its collision strength, we obtained ∼1.3/100. Some of the atomic lines may contaminate the C_{60} band fluxes. Our P-I model helps to estimate how the C_{60} bands are contaminated by the atomic lines. In particular, the C_{60} 7.0 μm flux is contaminated by the [Ar II] 6.99 μm line. We should bear in mind that the C_{60} 7.0 μm flux is important to discuss the excitation mechanism of C_{60} (see e.g. Bernard-Salas et al. 2012, for details). Therefore, first we need to correct the effective collision strength of the [Ar II] 6.99 μm. In the low-resolution *Spitzer*/IRS spectra, the C_{60} 18.9 μm flux is contaminated by the [S III] 18.67 μm line. This is in the case of Lin49. As we discuss later, the contamination of the C_{60} band fluxes except for the C_{60} 18.9 μm seems to be small.

In this modelling, we determine the intrinsic luminosity (L_*), the stellar radius (R_*), and the core mass (M_*) of the CSPN. We estimate the initial mass of the progenitor star by plotting the L_* and T_{eff} on theoretical evolutionary tracks of post-AGB stars. We also compare the ICFs from the P-I model with those calculated in Section 3.1.4.

3.4.1 Modelling approach

The distance to Lin49 is necessary for the comparison of the model with the observed fluxes and flux densities. Recent distance measurements to the SMC are 60.6 ± 2.9 kpc (Hilditch, Howarth & Harries 2005), 62.1 ±1.9 kpc (Graczyk et al. 2014), and 62.0 ± 0.6 kpc (de Grijs & Bono 2015, the distance was calculated from their distance modulus ($m-M$) = 18.96 ± 0.02). Using photometric data of red clump stars, Subramanian & Subramaniam (2009) investigated the line-of-sight (LOS) depth in the MCs. From their LOS depth map of the SMC and the location of Lin49 (this PN would be a bar member), the LOS 1σ depth towards Lin49 is in the range from 4 to 6 kpc, assuming an average value for the distance

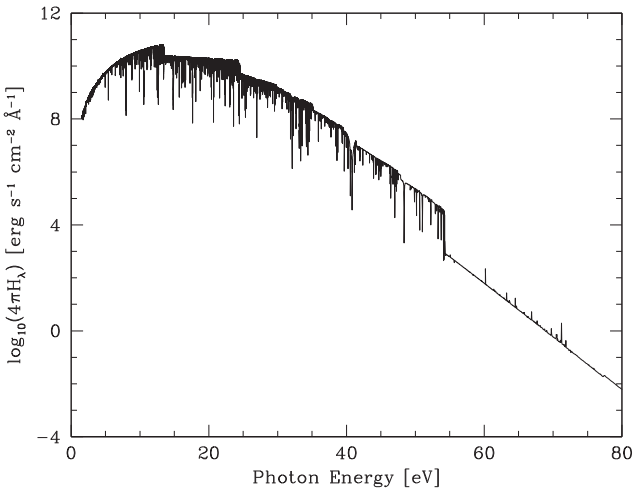

Figure 8. The SED of the CSPN synthesized by our TLUSTY modelling. We used this for the CLOUDY modelling as the incident SED of the CSPN.

of 60 kpc towards the SMC. Here we adopt the distance towards Lin49 to be 61.9 kpc, the average of the values above, weighted by the respective uncertainties, with a 1σ error in the average of ±5.0 kpc from the LOS depth.

We used the TLUSTY synthetic spectrum of the central star to define the ionizing/heating source as displayed in Fig. 8 (H_λ is the flux density of the stellar photosphere), while L_* is a free parameter.

Except for C, we adopt the results listed in Table 3 as initial guesses for the nebular elemental abundances, and refine these to match the observed line intensities of each element. As we explained in Section 3.1.6, we adopt and keep the *expected* CEL ϵ(C) of 8.46 throughout the model because we do not detect any C CELs constraining the CEL C abundance. For elements for which abundances could not be determined from nebular line analysis, we adopt the AGB nucleosynthesis model result of Fishlock et al. (2014) for stars with initial mass 1.25 $M_\odot$ and $Z = 0.001$.

Following the definition of Stanghellini et al. (1999) and Shaw et al. (2006) applied to MC PNe, we measure the photometric radius of Lin49 to be 0.23 arcsec, corresponding to the size of a circular aperture that contains 85 per cent of the flux in the z' band. We naturally consider the point spread function (FWHM ∼ 0.69 arcsec). We adopt a spherical shell nebula with uniform hydrogen density (n_H). Thus, we set the outer radius (R_{out}) to be 0.23 arcsec, where we define the ionization front.

A definition of the filling factor is the ratio of an rms density derived from an observed hydrogen line flux (e.g. Hα and Hβ), T_e, and nebula radius to the n_e(CELs) (see e.g. Mallik & Peimbert 1988; Peimbert, Peimbert & Ruiz 2000, for details). We calculate an rms density of 3600 cm^{-3} from the observed I(Hβ), T_e = 11 000 K, the radius = 0.23 arcsec, and a constant $n_e/n(H^+) = 1.15$. Thus, we estimate the filling factor to be around 0.5 using this rms density and the n_e([O II]).

We assume that the underlying continuum is due to graphite grains based on the fact that the nebula in Lin49 shows the spectral signature of carbon-rich species (i.e. fullerene). We use the optical data of Martin & Rouleau (1991) for randomly oriented graphite spheres, and assume the '1/3-2/3' approximation (for more details of this approximation, see Draine & Malhotra 1993). We adopt an MRN $a^{-3.5}$ size distribution (Mathis, Rumpl & Nordsieck 1977) with the smallest grain radius (a_-) = 0.005 μm and the largest radius (a_+) = 0.1 μm. We resolved the size distribution into 20 bins. We have not attempted to reproduce the 6–9 μm band and the broad

Table 7. Input parameters for the best fitting model and the derived properties by the CLOUDY model.

Parameters of the central star	Values
L_*	5916 $L_\odot$
R_*	2.73 $R_\odot$
M_*	0.53 $M_\odot$
$T_{\rm eff}$	30 500 K
M_V	−1.62
m_V	17.34
log g	3.29 cm s^{-2}
Distance	61.9 kpc
Parameters of the nebula	**Values**
Boundary condition	Ionization bound
$\epsilon(X)$	He:10.80/C:8.46/N:7.06/O:8.03, Ne:7.22/S:5.88/Cl:4.09/Ar:5.21, Fe:4.79/the others:Fishlock et al. (2014)
Geometry	Spherical
Shell size	$R_{\rm in}$ = 0.000 63 pc (130 au)
	$R_{\rm out}$ = 0.068 pc (1.42(+4) au)
$n_{\rm H}$	5080 cm^{-3}
Filling factor	0.50
$\log_{10}I(H\beta)$	−12.89 erg s^{-1} cm^{-2}
$m_{\rm g}$	0.11 $M_\odot$
Parameters of the dust	**Values**
Grain	Graphite only
Grain radius	0.005–0.10 μm
$T_{\rm d}$	See Fig. 9
$m_{\rm d}$	4.29(−5) $M_\odot$
$m_{\rm d}/m_{\rm g}$	3.97(−4)

11 μm/16–24 μm/30 μm features because the carriers of these features and their optical properties are not well known.

To find the best model, we use the VARY command of CLOUDY. This command allows us to vary parameter within a given range in order to match the observed values. In total, we varied 12 free parameters: L_*, the He/N/O/Ne/S/Cl/Ar/Fe abundances, $R_{\rm in}$, $n_{\rm H}$, and grain abundance until the χ^2 value calculated from the 51 gas emission fluxes, 4 broad-band fluxes (2MASS *JHKs* and IRAC bands were excluded), 3 far-IR flux densities at 65, 90, 120 μm, and the $I(H\beta)$ was minimized. The final χ^2 was 22.3.

In Table 7, we list the input parameters for the best fit and the properties derived by applying the model. The 1σ confidence interval of each elemental abundance is as follows: ϵ(He) = 0.02, ϵ(N) = 0.03, ϵ(O) = 0.02, ϵ(Ne) = 0.11, ϵ(S) = 0.02, ϵ(Cl) = 0.09, ϵ(Ar) = 0.06, and ϵ(Fe) = 0.13, respectively. We estimate the 1σ uncertainty of the $m_{\rm g}$, $m_{\rm d}$, and $m_{\rm d}/m_{\rm g}$ to be 0.02 $M_\odot$, 1.4(−6) $M_\odot$, and 6.8(−5) by taking the absolute *Spitzer*/IRS flux calibration uncertainty of ∼17 per cent (Decin et al. 2004) and the uncertainty of the distance.

In Table B4, we compare the observed and the model predicted values and list the predicted fluxes of important diagnostic lines such as the [C II] 157.6 μm for the more ionized plasma and the photodissociation region for the future studies. A discussion on the model results is presented in the following sections.

3.4.2 *Comments on the model results*

Assuming that the CSPN is in the midst of H-burning, comparing the estimated L_* and the measured $T_{\rm eff}$ on H-burning post-AGB evolution tracks with the initial Z=0.001 of Vassiliadis & Wood (1994) indicates a progenitor mass of 1.0–1.5 $M_\odot$, which is consistent with our interpretation in Section 3.1.8, where we concluded that Lin49 evolved from a 1.0–1.25 $M_\odot$ star based on elemental abundances. The conclusion on the initial mass does not change even in the two density composite model discussed in Section 4.1.2.

Table 8. The volume average ionization fraction of each element and comparison of the ICFs from the CLOUDY model and ones adopted in Section 3.1.4. The ICF(Obs) in He is derived from equation (A2). The ICF(Obs) in He based on the P-I model of M1-11 is 3.81 ± 0.22. The ICF(Obs) in C is for the RL ϵ(C).

X	X^0/X	X^+/X	X^{2+}/X	X^{3+}/X	ICF(CLOUDY)	ICF(Obs)
He	0.632	0.368			2.72	5.33±0.14
C		0.759	0.241		4.15	3.96±0.23
N	0.004	0.841	0.156		1.19	1.08±0.04
O	0.017	0.948	0.034		1.02	1.00
Ne	0.013	0.984	0.003		1.02	1.00
S		0.243	0.757		1.00	1.00
Cl		0.372	0.627		1.00	1.00
Ar	0.004	0.668	0.327		3.05	4.62±1.11
Fe		0.073	0.871	0.056	1.15	1.22±0.05

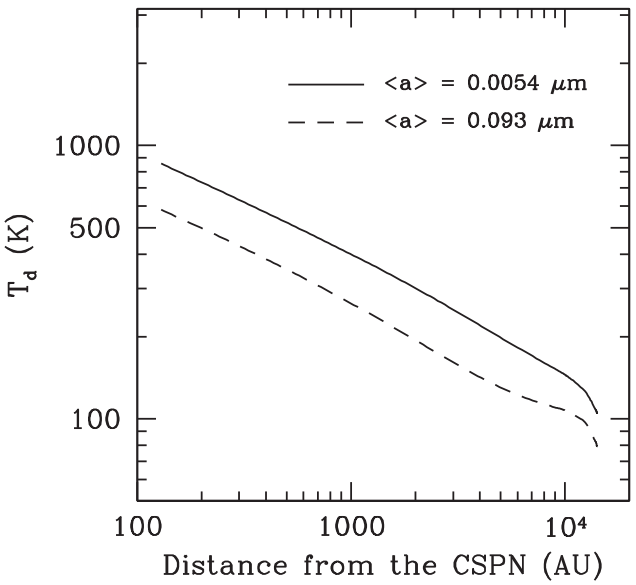

Figure 9. Radial temperature profiles of graphite grains in the smallest and largest size bins.

In Table 8, we list the volume-averaged ionization fraction of each element predicted by the CLOUDY model and the ICFs derived from those. The ICF(He) calculated from equation (A2), which is tuned for the H II regions, is overestimated and the ICF(He) = S/S^{2+} adopted for the PN M2-24 (Zhang & Liu 2003) may not be correct for Lin49 (see Appendix A1). For low ionization PNe, it is better to use the ICF(He) calculated by the P-I model. Since we do not include O^0 and N^0 in the elemental O and N abundances and we assume that Ne^0 is very small, their ICFs are slightly different from those of the model (0.02 in O and Ne and 0.11 in N).

The simulated dust temperature radial profiles are displayed in Fig. 9, where we plot the grain temperatures ($t_{\rm d}$) of the smallest and largest size bins. The size range of the smallest and largest bins is 0.0050–0.058 μm ($\langle a\rangle$ = 0.0054 μm) and 0.086–0.10 μm ($\langle a\rangle$ = 0.093 μm). The maximum and minimum $t_{\rm d}$ are 825 and 79 K.

Fig. 10(a) shows the synthesized mid-IR spectrum composed of atomic gas emission lines only based on the model result. By

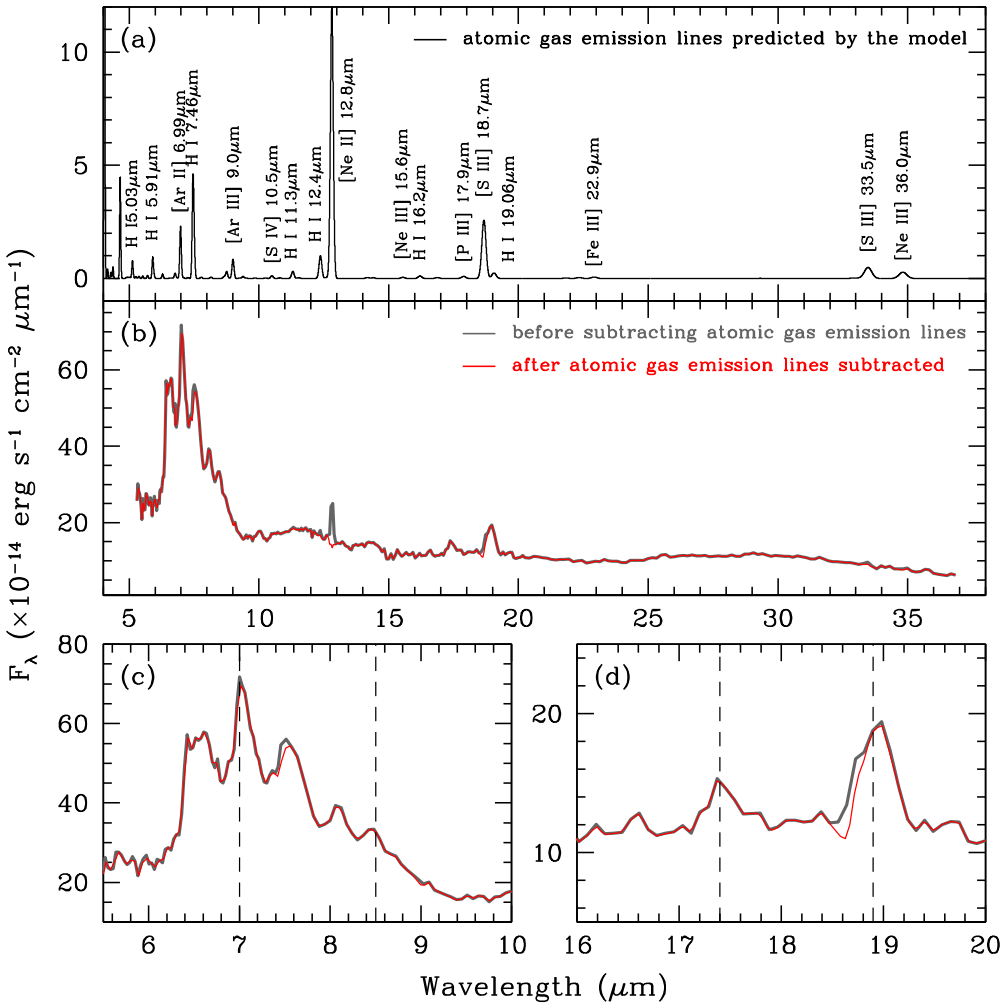

Figure 10. (a) The predicted atomic gas emission lines by the CLOUDY model. The resolution of this synthesized spectrum is 100, corresponding to that of *Spitzer*/IRS. (b) The original *Spitzer*/IRS spectrum (grey line) and the atomic line subtracted spectrum (red line). (c and d) Close-up plot of the four C_{60} bands, whose central wavelengths are indicted by the dashed vertical lines.

Table 9. Measurements of the four C_{60} bands before('B')/after('A') subtracting the synthesized mid-IR spectrum presented in Fig. 10(a).

Band	λ_c(B) (μm)	FWHM(B) (μm)	F(B) (erg s^{-1} cm^{-2})	λ_c(A) (μm)	FWHM(A) (μm)	F(A) (erg s^{-1} cm^{-2})	(F(A) − F(B)) /F(B) (per cent)
7.0 μm	7.04 ± 0.01	1.97(−1) ± 3.26(−3)	5.14(−14) ± 9.50(−16)	7.04 ± 0.01	1.98(−1) ± 3.22(−3)	4.99(−14) ± 9.80(−16)	3.0
8.5 μm	8.47 ± 0.01	1.61(−1) ± 2.29(−2)	7.41(−15) ± 7.43(−16)	8.47 ± 0.01	1.57(−1) ± 2.14(−2)	7.18(−15) ± 8.54(−16)	3.1
17.4 μm	17.42 ± 0.02	3.27(−1) ± 3.90(−2)	1.05(−14) ± 1.30(−15)	17.42 ± 0.01	3.23(−1) ± 5.67(−2)	1.05(−14) ± 1.70(−15)	0.5
18.9 μm	18.92 ± 0.01	3.76(−1) ± 2.42(−2)	2.86(−14) ± 2.00(−15)	18.95 ± 0.01	3.18(−1) ± 1.68(−2)	2.51(−14) ± 1.40(−15)	12.3

subtracting this generated spectrum from the observed *Spitzer*/IRS spectrum, we can see how the four C_{60} bands are contaminated with atomic lines, in particular, [Ar II] 6.99 μm and [S III] 18.67 μm lines and we can obtain more accurate measurements of these C_{60} bands. Fig. 10(b) shows the original *Spitzer*/IRS spectrum (grey line) and the atomic line subtracted spectrum (red line). We focus on the C_{60} bands in Figs 10(c) and (d). In Table 9, we summarize the measurements of the four C_{60} bands before('B')/after('A') subtracting the synthesized mid-IR spectrum presented in Fig. 10(a). Accordingly, we confirm that the line contribution is very small except for the 18.9 μm C_{60} band; compared to the result before subtracting atomic gas emission contributions (mainly [S III] 18.67 μm), its central wavelength (λ_c) is shifted towards red wavelengths, FWHM is much narrower, and the flux is smaller.

In Fig. 11(a), we present the observed SED plots (grey circles and lines) and the modelled SED (red line). The three grey diamonds in far-IR are the fluxes predicted by the broad 30 μm fitting. In Fig. 11(b), we display a close-up of the SED in the wavelength range covered by the *Spitzer*/IRS spectrum. The simulated SED cannot fit the NIR observed data. This strong NIR excess in Lin49 is also impossible to fit by models with amorphous carbon. The NIR excess is better revealed in Fig. 12, where we show the residual spectra (grey lines) and photometry points (blue filled circles) obtained by making the difference between the observations and the CLOUDY model values.

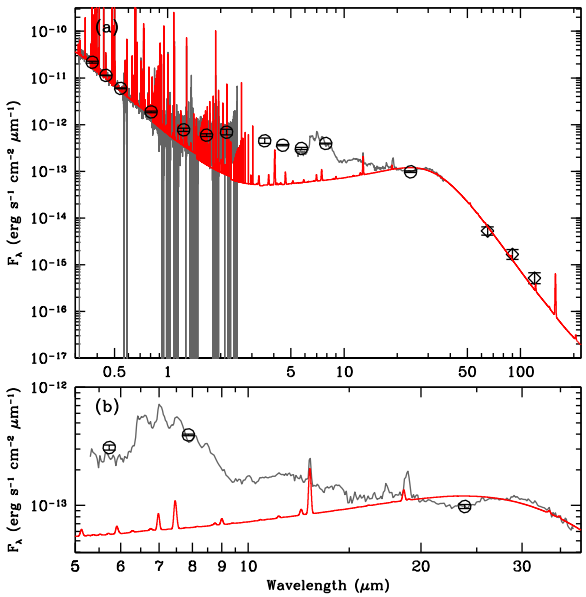

Figure 11. SED of Lin49. (a) Comparison between the CLOUDY model SED (red line) and the observational data. The spectral resolution of the gas emission lines is constant and assumes the following values: 1000 in $\lambda <$ 0.3 μm, 9200 in $\lambda =$ 0.3–1.0 μm, 4800 in $\lambda =$ 1.0–2.5 μm, and 100 in $\lambda >$ 2.5 μm. The observed spectral and photometric data (XSHOOTER, MCPS *UBVI* bands, 2MASS *JHKs* bands, and *Spitzer*/IRAC 4 bands and MIPS 24 μm band) are also plotted (grey lines and black circles). The XSHOOTER, MCPS, and 2MASS data are de-reddened values with $c(\mathrm{H}\beta) = 0.11$ and $R_V = 3.1$. The squares at 65, 90, 120 μm are the average *expected* flux density obtained from Fits 1 and 2 in Section 3.3. (b) Close-up plot for mid-IR wavelengths. See the text for details.

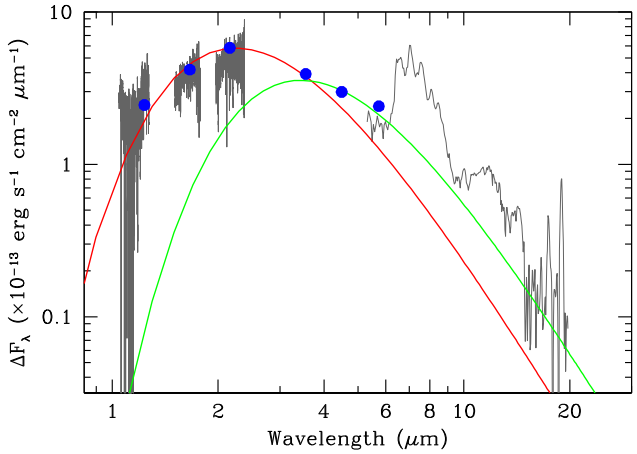

Figure 12. NIR excess. The grey lines and the blue dots are the residual flux densities (ΔF_λ) between the observed XSHOOTER/IRS spectra and 2MASS *JHKs*, IRAC 3.6/4.5/5.8 μm photometry bands and the corresponding values obtained from the CLOUDY model. In the XSHOOTER and IRS spectra, we block the spectral regions except for 1.046–1.271 μm (*J*), 1.508–1.778 μm (*H*), 1.974–2.377 μm (*Ks*), and 5.31–19.74 μm. The red line is the best fit of this NIR excess with a Plank function with a single temperature of 1250 K. The green line is another Plank function fitted with the fixed 861 K. The ΔF_λ in the photometry bands are listed in Table 10. See the text in Section 4.1.

Table 10. The residual flux densities (ΔF_λ) between the observed 2MASS *JHKs* and *Spitzer*/IRAC 3.6/4.5/5.8 μm bands and the corresponding values obtained from the CLOUDY model.

Band	λ_c (μm)	ΔF_λ (erg s^{-1} cm^{-2} μm^{-1})
2MASS *J*	1.235	2.83(−13)
2MASS *H*	1.662	4.32(−13)
2MASS *Ks*	2.159	5.87(−13)
IRAC-Band1	3.600	3.96(−13)
IRAC-Band2	4.500	3.06(−13)
IRAC-Band3	5.800	2.51(−13)

4 DISCUSSION

4.1 Interpretations for the NIR excess

4.1.1 Stochastic heating of extremely small particles

For the usual dust grain sizes (e.g. $\gtrsim$0.01 μm), dust temperatures are determined by solving an energy balance equation between the radiative heating owing to the central star and the cooling of grains. For such grain sizes, individual quantum events are not important. However, for very small grains, which are composed of 100 atoms or less, single photons would cause them to heat up significantly for very short time-scales. This mechanism is known as stochastic heating (or quantum heating), and has been proposed to explain the spectra of the reflection nebulae NGC 7023 and NGC 2023 (Sellgren 1984), and the PNe IC418 (Phillips, Sanchez Magro & Martinez Roger 1984) and Abell 58 (Koller & Kimeswenger 2001). Interestingly, these reflection nebulae and IC418 show mid-IR C_{60} band emission. We included the stochastic heating mechanism in CLOUDY model, as is default for CLOUDY. However, our model cannot fit the observed SED in the ∼1–5 μm wavelength range at all.

For the residual data plots in Fig. 12, it is possible to fit the excess with a Planck function with a single temperature of 1250 ± 42 K (indicated by the red line). The residual flux densities (ΔF_λ) in the photometry bands are listed in Table 10. The luminosity and the minimum emitting radius of this component are 290 ± 80 $L_\odot$ and ∼2 au. According to Sellgren (1984) and Whittet (2003), the thermal properties of solids are described by Debye's theory and the heat capacity C_V for T over Debye temperature Θ (in graphite, Θ is ∼500 K) is $3Nk$, where N is the number of the atoms in a molecule and $3N$ is its number of degrees of freedom. For extremely small grains, an average absorbed photon energy $E_{\rm ph}$ produces the difference between the maximum and minimum temperatures ΔT written by the following equation:

$$\Delta T = \frac{E_{\rm ph}}{3Nk}. \quad (5)$$

The $T_{\rm eff}$ of the central star is 30 500 K, so the photon energy at the radiation peak is 13.05 eV (Fig. 8). $E_{\rm ph}$ could be lower than 13.05 eV. Thus, we obtained $\Delta T < 5.05(+4)/N$.

By adopting the maximum and minimum temperatures of 1250 and 20 K, we obtain a value for N of $\lesssim$39, although our estimation is very optimistic and also depends on the minimum temperature. If such a molecule formed as a honeycomb structure sheet is distributed in the nebula, the molecule's dimension is roughly ∼8(−4) μm × 8(−4) μm square. If the molecule is a cage not a sheet, e.g., fullerene C_{36}, the size would be small; in the case of C_{36}, the approximate diameter is 5(−5) μm (Piskoti, Yarger & Zettl 1998). The SED with ΔT of 841 K derived by keeping N of

60 (indicated by the green line) gives a better fit to the differential spectrum in $\gtrsim$3.6 μm.

A top-down mechanism has been suggested for the formation of C_{60}; C_{60} could be formed from the shrinkage of larger molecules, e.g. from larger clusters of PAHs (Zhen et al. 2014; Berné, Montillaud & Joblin 2015), or HAC (Duley & Hu 2012). PAH clusters could form from HACs. Scott, Duley & Pinho (1997a) showed that $C_{50,60,70}$ may be produced by the decomposition of HACs. As explained in Section 2.2, the 6–9 μm band profile in Lin49 is very similar to the thermal emission profile of HAC as presented in fig. 2 of Scott et al. (1997b). Molecules composing of $\lesssim$39 C-atoms might be a by-product in the decomposition process of HACs.

As a pragmatic problem, with grains composing of $\lesssim$39 C-atoms only, it could be difficult to reproduce the observed broad continuous NIR excess feature seen in Lin49; to get a continuum-like behaviour, enough interacting vibrational modes are necessary. Therefore, we need to examine other possible explanations for NIR excess in Lin49.

4.1.2 High-density structure nearby the CSPN

In Section 3.4, we assumed that Lin49 does not have any sub-structures surrounding the CSPN but that this PN has a normal density nebula. However, the minimum emitting radius of the 1250 K blackbody component suggests that the NIR component could be emitted by a sub-structure near the central star. A similar idea was proposed for the NIR excess at the central position of IC418; Hora et al. (1993) took the NIR *JHK* images of this PN and found excess at the central position after subtracting the contribution from the central star. The authors argued that the excess indicates a possible compact shell interior to the main shell.

Lin49 may also have a central dense structure, which will be responsible for its NIR excess. To test this hypothesis, we construct a two-shell model. The model is composed of an outer low-density shell and an inner high-density shell. For the dust distribution on the high-density shell, we assume that the dust is composed of graphite grains with an $a^{-3.5}$ size distribution, where $a = 0.005$–0.1 μm. $R_{\rm out}$ for this shell corresponds to the $R_{\rm in}$ for the outer, low-density shell. The P-I model for the low-density shell has already been constructed in Section 3.4, with the residual SED indicating the NIR excess as presented in Fig. 12.

We fit the residual SED in the wavelength range from 1 to 5 μm using CLOUDY. In this process, we keep the following parameters derived in the low-density shell model: the filling factor, the elemental abundances and the dust composition/size distribution/abundance, and L_*. As the luminosity of the NIR excess component is small compared to that of the central star (<5 per cent of L_*), we will minimize the number of free parameters by initially fixing L_* (later this value will be fine-tuned). The free parameters are $R_{\rm in}$ and n(H), which are determined through fitting the residual 1–5 μm SED.

We combine the radial n(H) profiles of the low- and high-density shells into one (see Fig. 13), and run the model with this n(H) profile to match the observed SED plots in UV to far-IR wavelength. For fine-tuning, we allow an increase of L_* by 10 per cent and a slight increase of the elemental abundances, except for C.

Finally, we obtained the predicted SED as presented in Fig. 14, which better fits the 1–5 μm wavelength rage, compared to Fig. 11. The χ^2 was 37 calculated from the 51 gas emission fluxes, 9 broad-band fluxes, 3 far-IR flux densities at 65, 90, 120 μm, and the $I(\mathrm{H}\beta)$. In the fourth and ninth columns of Table B4, we compare the observed and model predicted values and list the predicted fluxes.

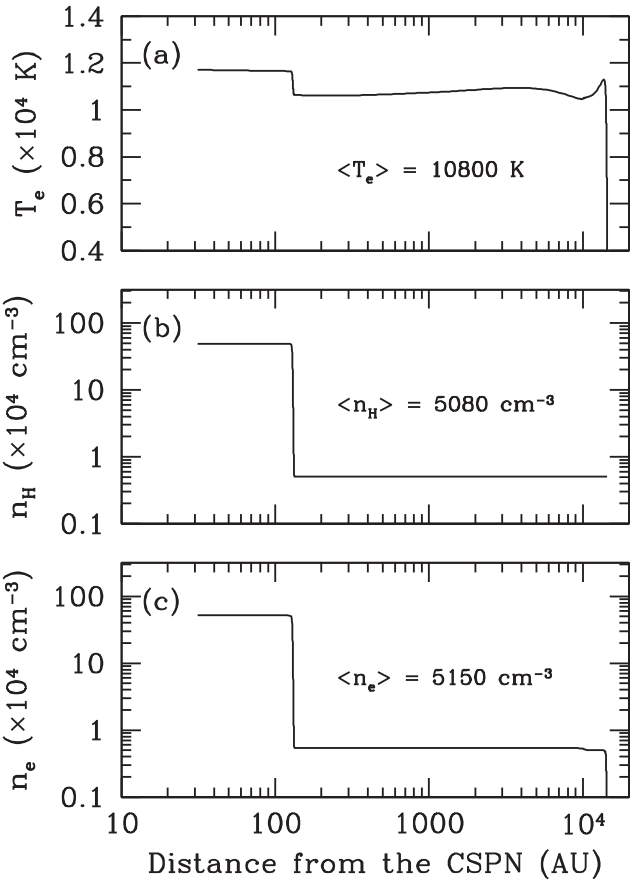

Figure 13. Radial profiles of the $T_{\rm e}$ (a), n(H) (b), and $n_{\rm e}$ (c) predicted by the two density shell model. The averaged value of each physical parameter is indicated in each panel.

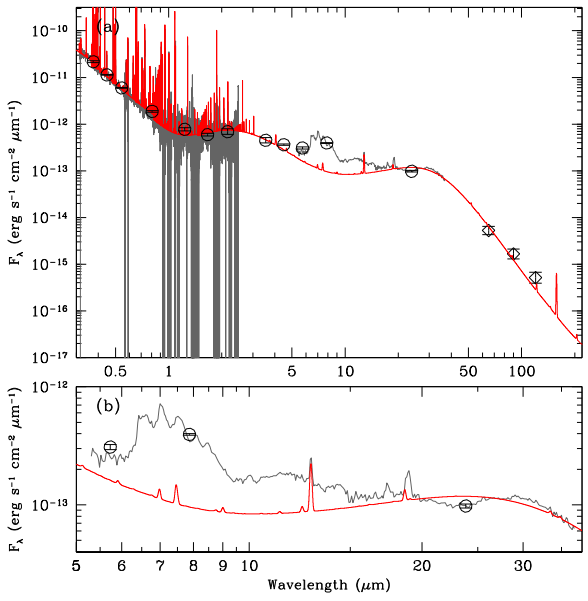

Figure 14. (a) Comparison between the observed SED plots and the predicted SED by the two density shell model. The spectral resolution of the gas emission lines is a constant 1000 in <0.3 μm, 9200 in 0.3–1.0 μm, 4800 in 1.0–2.5 μm, and 100 in >2.5 μm. (b) Close-up plot for mid-IR wavelengths. The lines and symbols in both of panels are as defined in Fig. 11.

Table 11. Input parameters of the best fitting model in the two-shell model and the derived properties.

Parameters of the central star	Values
L_*	6333 $L_\odot$
R_*	2.84 $R_\odot$
M_*	0.57 $M_\odot$
$T_{\rm eff}$	30 500 K
M_V	−1.70
m_V	17.26
log g	3.29 cm s^{-2}
Distance	61.9 kpc
Parameters of the nebula	**Values**
Boundary condition	Ionization bound
$\epsilon(X)$	He:10.80/C:8.46/N:7.06/O:8.03, Ne:7.27/S:5.88/Cl:4.08/Ar:5.22, Fe:4.71/the others:Fishlock et al. (2014)
Geometry	Spherical
Shell size	$R_{\rm in}$ = 0.000 15 pc (31 au)
	$R_{\rm out}$ = 0.068 pc (1.42(+4) au)
$n_{\rm H}$	See Fig. 13
Filling factor	0.50
$\log_{10}I({\rm H}\beta)$	−12.89 erg s^{-1} cm^{-2}
$m_{\rm g}$	0.11 $M_\odot$
Parameters of the dust	**Values**
Grain	Graphite only
Grain radius	0.005–0.10 μm
$T_{\rm d}$	See Fig. 15
$m_{\rm d}$	4.15(−5) $M_\odot$
$m_{\rm d}/m_{\rm g}$	3.86(−4)

The input parameters for the best-fitting model and the derived parameters are summarized in Table 11.

Since we increased L_* to obtain the best fit, the core mass of the CSPN is 0.57 $M_\odot$, accordingly. As we argued before, even in this core mass, our conclusion on the initial mass of the progenitor star does not change. The predicted elemental abundances in the two-shell model are almost consistent with the single-shell model in Section 3.4. The 1σ of the elemental abundances and the $m_{\rm g}$, $m_{\rm d}$, and $m_{\rm d}/m_{\rm g}$ is almost same value discussed in Section 3.4. The radial profiles of $T_{\rm e}$, n(H), and $n_{\rm e}$ are presented in Fig. 13. The value for $n_{\rm e}$ of the high-density shell is very high. However, the emitting volume of the high-density shell is very small. Therefore, the volume-averaged $n_{\rm e}$ (5150 cm^{-3}) is not over the observed one.[8] The radial $t_{\rm d}$ profile is presented in Fig. 15. The maximum temperature of the $\langle a\rangle = 0.0054$ μm grains (1450 K) meets the requirement to fit the residual 1–5 μm SED plots but is not over the evaporation temperature of graphite.

Thus, we succeeded in explaining the NIR excess by postulating the existence of a high-density structure nearby the CSPN. If we can believe that the NIR excess emits from this high-density structure, how did the progenitor form this during its evolution?

4.1.3 Does Lin49 have a disc?

We suggest that the NIR emission does not originate from the nebular shell, but from a disc around the central star. According to the review by van Winckel (2003), the hot dust component (∼1000 K) in some post-AGB stars (first noticed by Trams et al. 1991) was interpreted as evidence for significant post-AGB mass-loss. However, this interpretation became untenable because dusty post-AGB mass-loss would speed up the evolution such that very few objects would be observable (Trams et al. 1989). At present, the most accepted formation mechanism to produce a disc around an evolved star is the binary model (e.g. Kwok, Hrivnak & Su 2000, and references therein). This model states that PNe with a disc around the central star evolve from a binary system that went through a common envelope phase. During this phase, the secondary star induces the mass-loss of the AGB star to occur preferentially in the orbital plane, which gives birth to a disc. Thus, if the presence of a disc is confirmed around the central star of Lin49, this is a strong indication that this PN evolved from a binary system. The binary disc could stably harbour the NIR emitters near the central star for a long time.

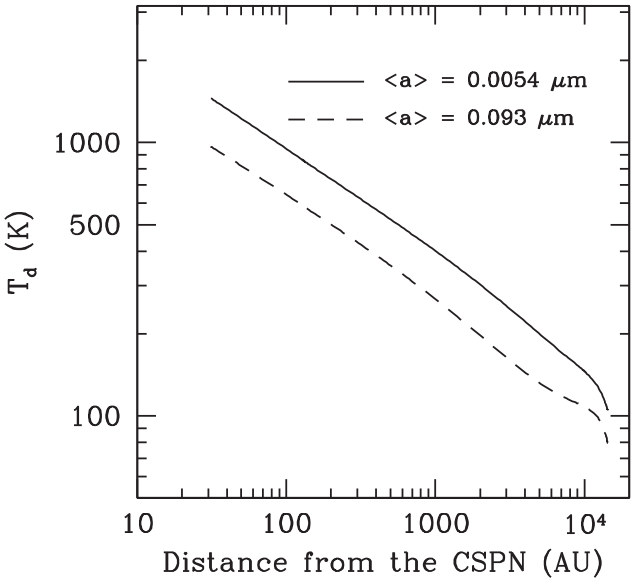

Figure 15. Radial temperature profiles of graphite grains in the smallest and largest size bins predicted by the two-shell model.

Kamath, Wood & Van Winckel (2014) classified 63 SMC objects into post-AGB/red giant branch (RGB) candidates based on their SEDs in the optical to mid-IR, and they reported that 21 objects out of these are post-AGB stars and 27 show a strong NIR excess interpreted as the presence of a circumbinary disc. Maas, Van Winckel & Lloyd Evans (2005) investigated elemental abundances of the Galactic 12 post-AGB stars showing NIR excess (they interpreted as the presence of a disc); nine of them are affected by the depletion process, that is, elements with a high condensation temperature (e.g. Fe) are largely depleted and get locked in dust grains whereas elements with a low temperature remain in gas phase. Since the temperature in the disc decreases with increasing radius, at the inner radius of the disc only the elements with a high condensation temperature are caught in grains, given that the inner temperature of the disc is high. Maas et al. (2005) indicated that the presence of the depletion process and the presence of a disc are linked.

From the observational results of Kamath et al. (2014) and Maas et al. (2005), the strong NIR excess and the strongly depleted *nebular* Fe abundance in Lin49 might be explained by the presence of a disc. Most of the Fe-atoms might be tied up in dust grains (e.g. FeO) within a disc. If Lin49 has a disc, the large carbon molecules such as fullerene were relatively easily formed.

[8] XSHOOTER could not resolve Lin49 and this instrument looks at the average light of this PN in each wavelength. The Paschen line analysis could suggest the presence of such high-density shell indirectly.

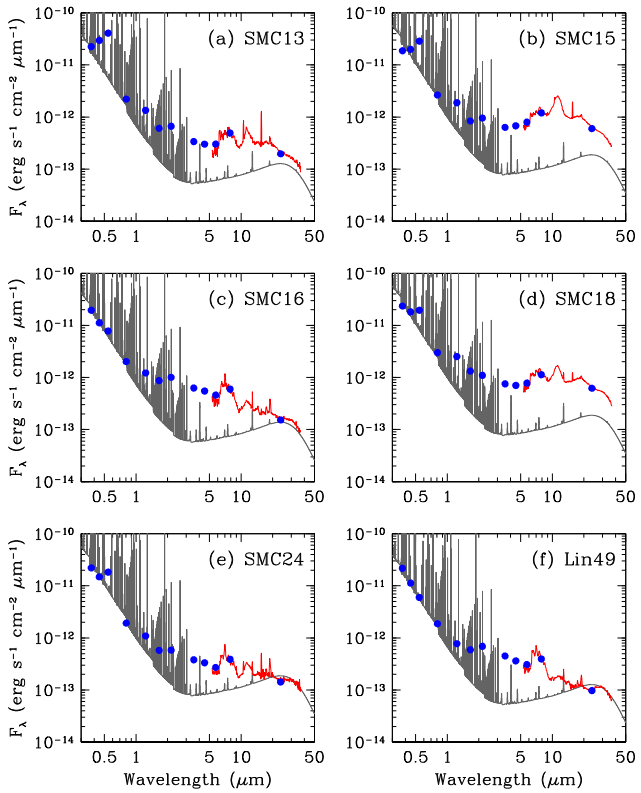

Figure 16. SED plots of SMC C_{60} PNe SMC13, 15, 16, 18, 24, and Lin49. The blue filled circles are the de-reddened photometric data. In each panel, we compare with the resultant SED of Lin49 synthesized in Section 3.4. Note that in each panel Lin49's SED is scaled to the observed de-reddened flux density of each PN at the I_c band.

4.1.4 NIR excess in SMC C_{60} PNe and counterparts

Is the NIR excess seen in other SMC C_{60} PNe? Amongst SMC C_{60} PNe, SMP24 also shows an NIR excess. By applying an SED fit over the range from the *B* band to ∼1.337 GHz, Bojicic, Filipovic & Crawford (2010) find that a hotter dust component (∼1000 K) is necessary to fit the observed SED down to 1 μm, apart from the hot dust component (∼270 K).

The photometric data from MCPS, 2MASS, and *Spitzer*/IRAC and MIPS, and the *Spitzer*/IRS spectra of the SMC C_{60} PNe are plotted in Fig. 16. As no optical data are available for SMC1, this source was not included in the figure. According to Table 4, the effective temperatures of the SMC C_{60} PNe are in the range between 30 500 and 58 000 K, and the average $T_{\rm eff}$ amongst these PNe except for SMC15 (58 000 K) is 34 100 K. The observed UV–optical wavelength SEDs in these PNe are not largely different from each other, except for SMC15. Thus, we plot the resultant synthesized SED of Lin49 (Section 3.4) as the comparison; in each panel, this Lin49's SED is scaled to the observed de-redden flux density of each PN at the I_c band.

Amongst C_{60} PNe, the SEDs of SMC16 and SMC24 are very similar to that of Lin49; their SEDs have a flux density peak around 2MASS *Ks* band and the NIR excess features are apparently as broad as that seen in Lin49. SMC13, 15, and 18 do not show such a broad NIR excess as seen in Lin49. However, their SED slope in the range from *U* to I_c band wavelength is different from those in the range from 2MASS to IRAC band wavelength.

In Fig. 17, we show the SEDs of non-C_{60} C-rich PNe, SMC6 and SMC27. From Table B5, they are selected as comparison objects to

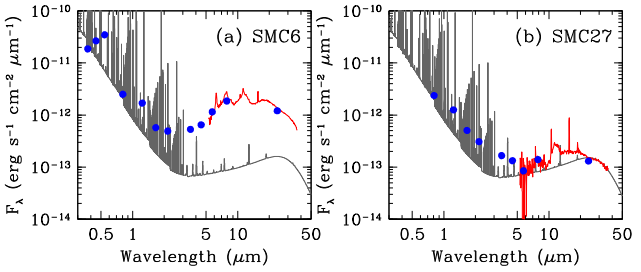

Figure 17. SED plots of non-C_{60} C-rich SMC PNe SMC6 and 27. The lines and symbols in both of panels are as defined in Fig. 16.

Table 12. The average elemental abundances of C_{60}-containing PNe and non-C_{60} C-rich PN in the SMC and the Milky Way (MW). The data of the SMC PNe are taken from Tables 4 and B5. The data of the MW PNe are from tables 3 and 4 of Otsuka et al. (2014).

PNe	ϵ(C)	ϵ(N)	ϵ(O)	ϵ(Ne)	ϵ(S)	ϵ(Ar)
SMC C_{60} PNe	8.28	7.17	7.97	7.07	6.54	5.64
Lin49	8.46	6.93	8.11	7.18	6.02	5.48
SMC C-rich PNe	8.67	7.37	8.08	7.28	6.69	5.64
MW C_{60} PNe	8.73	7.81	8.48	7.85	6.45	5.98
MW C-rich PNe	8.85	8.23	8.56	8.06	8.05	6.85

the C_{60} SMC PNe because the $T_{\rm eff}$s of SMC6 and SMC27 are close to those of SMC C_{60} PNe. We excluded SMC11 as a comparison because Villaver et al. (2004) reported $T_{\rm eff}$ of 40 900 K whereas we confirmed that its SED in the range from MCPS *B* (no m_U) to IRAC bands has a peak around I_c band and it can be well expressed by a single Planck function with the temperature of 3722 K, indicating that this object could not be a PN.

Although it is hard to draw a strong conclusion based on the photometric data points and mid-IR spectra only, SMC C_{60} PNe seem to show an NIR excess component to lesser or greater degree. This suggests that these C_{60} PNe might maintain a structure near their central star. Meanwhile, we do not find a flux density peak around 2MASS *Ks* in SMC non-C_{60} PNe SMC6 and 27. To reach a firm conclusion, we need to obtain NIR spectra in order to check whether or not each PN displays an NIR excess.

4.2 Comparison of physical properties between C_{60} PNe and non-C_{60} C-rich PNe

In Table 12, we summarize the average elemental abundances of SMC and MW C-rich PNe. In Section 3.1.8, from the view of elemental abundances, we concluded that Lin49 and the other SMC C_{60} PNe evolved from the initially 1.0–1.25 $M_\odot$ stars by comparing with the AGB nucleosynthesis results of Fishlock et al. (2014). The lowest S and Ar abundances of Lin49 amongst SMC C_{60} PNe indicate that this PN is an older population in the SMC. While there are no large differences in S and Ar (because these are Type II SN products), we found that the C, N, and Ne in SMC non-C_{60} PNe are greater than those in SMC C_{60} PNe, indicating that non-C_{60} PNe evolved from more massive stars. The C and Ne are synthesized in the He-rich intershell during the thermal pulse AGB phase, and these elements together with N and *n*-capture elements are brought up to the stellar surface by the third dredge-up (TDU). The efficiency of TDU depends on the initial mass and composition and increases as larger initial mass (e.g. Karakas 2010). The rich Ne in non-C_{60} PNe would be due to the double α capturing by rich ^{14}N. Certainly, the average abundances in SMC non-C_{60} PNe are close to the AGB

model result for the 1.25 and 1.50 $M_\odot$ stars rather for the 1.0 and 1.25 $M_\odot$ stars.

Otsuka et al. (2014) argued that elemental abundances of MW C_{60} PNe can be explained by AGB models for 1.5–2.5 $M_\odot$ stars with the SMC metallicity (i.e. $Z = 0.004$). Although there is a sample selection bias, the C, N, and Ne abundances in the non-C_{60} MW C-rich PNe indicate that these PNe evolved from more massive stars. Thus, at this moment, we might conclude that the progenitors of C_{60} PNe in both the SMC and the MW are not greater than those of non-C_{60} PNe.

Otsuka et al. (2013, 2014) reported that the MW C_{60} PNe have cool central stars. The average $T_{\rm eff}$ amongst MW C_{60} PNe calculated from table 3 of Otsuka et al. (2014) is 37 780 K, which is in excellent agreement with the average $T_{\rm eff} = 38\,770$ K amongst the SMC C_{60} PNe (see Table 4). The $T_{\rm eff}$ of Lin49 is the coolest amongst SMC C_{60} PNe. Taking their average ionized nebula radius r of 0.17 arcsec (0.05 pc in linear scale), SMC C_{60} PNe are slower evolving objects than SMC non-C_{60} PNe, where the average $T_{\rm eff}$ is 72 100 K and the average r is 0.34 arcsec (0.10 pc in linear scale).

5 SUMMARY AND FUTURE WORKS

We performed a detailed spectroscopic analysis of the fullerene C_{60}-containing PN Lin49 in the SMC. We derived the nebular abundances of the nine elements. Compared to the [S,Ar/H] abundances, the [Fe/H] value is extremely low. Applying the predictions of the [S,Ar/Fe] abundances at [Fe/H] < -1 by the chemical evolution model for the MW halo, the [Fe/H] in Lin49 was originally ~ -1.4, indicating that the metallicity (Z) was $\sim$0.0006 ($\sim 0.04\,Z_\odot$) and that > 96 per cent of the Fe-atoms are trapped in Fe-rich dust grains. The nebular abundances are in good agreement with the AGB nucleosynthesis model for stars with an initial mass 1.25 $M_\odot$ and $Z = 0.001$ of Fishlock et al. (2014), even taking into account that the *expected* CEL ϵ(C) is 8.46.

We derived stellar abundances, effective temperature, and surface gravity. From the nebular and stellar C/O ratio abundances and the observed dust features, Lin49 is certainly a C-rich PN. We construct a P-I model in order to investigate the physical conditions of the central star, nebula, and dust grains and derive the gas and dust masses. The current core mass of the CSPN is 0.53–0.57 $M_\odot$, and theoretical evolution tracks of post-AGB stars indicate that it was initially 1.0–1.5 $M_\odot$. Taking the elemental abundances into account, we conclude that Lin49 evolved from 1.0–1.25 $M_\odot$. Our model with the 0.005–0.1 μm radius graphite grains and a constant hydrogen density shell cannot fit the $\sim$1–5 μm part of the SED due to a prominent NIR excess, whereas in the other wavelengths the model gave a reasonable fit to the observed fluxes of nebular lines and broad-band fluxes/flux densities.

The NIR excess might possibly be due to either (1) the presence of small carbon clusters, small graphite sheet, and also fullerene precursors, or (2) the presence of high-density structure surrounding the central star. Taking the observational results of C_{60} PN IC418 in the MW and post-AGB/RGB stars in the SMC, and the extremely Fe-depletion in Lin49 into account, the latter option seems to be a better interpretation for Lin49's NIR excess.

In addition to Lin49, we find that other SMC C_{60} PNe also show an NIR excess component to lesser or greater degree based on their UV to mid-IR photometry data and *Spitzer*/IRS spectra. We suggest that these C_{60} PNe might maintain a structure near their central star as a stable producing source of the NIR excess in these PNe. Such a structure might be a circumbinary disc and it might play a role in C_{60} formation in evolved stars. NIR spectroscopy and monitoring observations of SMC C_{60} PNe might confirm the NIR excess and whether these PNe have binary central stars. Such observations would be important to understand the nature of the C_{60} PNe, the evolution of their central stars, and the formation of the C_{60} in the circumstellar environment.

ACKNOWLEDGEMENTS

This work is based on observations made with ESO Telescopes at the Paranal Observatory under programme ID 091.C-0934(B) (PI: Lex Kaper) during Amsterdam GTO time. We are grateful to the anonymous referee for carefully reading the manuscript and making useful suggestions which greatly improved this paper. MO was supported by the research fund 104-2811-M-001-138 and 104-2112-M-001-041-MY3 from the Ministry of Science and Technology (MOST), R.O.C. FK also acknowledges financial support from MOST, under grant numbers MOST103-2112-M-001-033- and MOST104-2628-M-001-004-MY3. MO and FK thank the IAA ICSM group members for fruitful discussions. MLL-F was supported by CNPq, Conselho Nacional de Desenvolvimento Científico e Tecnológico - Brazil, process number 248503/2013-8. Studies of interstellar chemistry at Leiden Observatory are supported through the advanced-ERC grant 246976 from the European Research Council, through a grant by the Dutch Science Agency, NWO, as part of the Dutch Astrochemistry Network, and through the Spinoza prize from the Dutch Science Agency, NWO. JBS wishes to acknowledge the support of a Career Integration Grant within the 7th European Community Framework Program, FP7-PEOPLE-2013-CIG-630861-SYNISM. This work was partly based on archival data obtained with the *Spitzer Space Telescope*, which is operated by the Jet Propulsion Laboratory, California Institute of Technology under a contract with NASA. Support for this work was provided by an award issued by JPL/Caltech. A portion of this work was based on the use of the ASIAA clustering computing system.

REFERENCES

Aller L. H., Keyes C. D., Maran S. P., Gull T. R., Michalitsianos A. G., Stecher T. P., 1987, ApJ, 320, 159
Asplund M., Grevesse N., Sauval A. J., Scott P., 2009, ARA&A, 47, 481
Begemann B., Dorschner J., Henning T., Mutschke H., Thamm E., 1994, ApJ, 423, L71
Benjamin R. A., Skillman E. D., Smits D. P., 1999, ApJ, 514, 307
Benjamin R. A., Skillman E. D., Smits D. P., 2002, ApJ, 569, 288
Bernard-Salas J., Peeters E., Sloan G. C., Gutenkunst S., Matsuura M., Tielens A. G. G. M., Zijlstra A. A., Houck J. R., 2009, ApJ, 699, 1541
Bernard-Salas J., Cami J., Peeters E., Jones A. P., Micelotta E. R., Groenewegen M. A. T., 2012, ApJ, 757, 41
Berné O., Montillaud J., Joblin C., 2015, A&A, 577, A133
Bohlin R. C., Colina L., Finley D. S., 1995, AJ, 110, 1316
Bojicic I. S., Filipovic M. D., Crawford E. J., 2010, Serb. Astron. J., 181, 63
Cami J., Bernard-Salas J., Peeters E., Malek S. E., 2010, Science, 329, 1180
Cardelli J. A., Clayton G. C., Mathis J. S., 1989, ApJ, 345, 245
Costa R. D. D., de Freitas Pacheco J. A., Idiart T. P., 2000, A&AS, 145, 467
Davey A. R., Storey P. J., Kisielius R., 2000, A&AS, 142, 85
de Grijs R., Bono G., 2015, AJ, 149, 179
Decin L., Morris P. W., Appleton P. N., Charmandaris V., Armus L., Houck J. R., 2004, ApJS, 154, 408
Delgado-Inglada G., Rodríguez M., 2014, ApJ, 784, 173
Delgado-Inglada G., Morisset C., Stasińska G., 2014, MNRAS, 440, 536
Dennefeld M., 1989, in de Boer K. S., Spite F., Stasińska G., eds, Recent Developments of Magellanic Cloud Research. Observatoire de Paris, Section Astrophysique de Meudon, Meudon, France, p. 107
Dopita M. A., Meatheringham S. J., 1991a, ApJ, 367, 115

Dopita M. A., Meatheringham S. J., 1991b, ApJ, 377, 480
Dopita M. A., Lawrence C. J., Ford H. C., Webster B. L., 1985, ApJ, 296, 390
Draine B. T., Malhotra S., 1993, ApJ, 414, 632
Duley W. W., Hu A., 2012, ApJ, 745, L11
Escalante V., Morisset C., Georgiev L., 2012, MNRAS, 426, 2318
Fang X., Liu X.-W., 2011, MNRAS, 415, 181
Ferland G. J., Korista K. T., Verner D. A., Ferguson J. W., Kingdon J. B., Verner E. M., 1998, PASP, 110, 761
Fishlock C. K., Karakas A. I., Lugaro M., Yong D., 2014, ApJ, 797, 44
Fitzpatrick E. L., 1986, AJ, 92, 1068
Garcia-Hernandez D. A., 2015, IAU General Assembly, 22
García-Hernández D. A., Manchado A., García-Lario P., Stanghellini L., Villaver E., Shaw R. A., Szczerba R., Perea-Calderón J. V., 2010, ApJ, 724, L39
García-Hernández D. A. et al., 2011, ApJ, 737, L30
García-Hernández D. A., Villaver E., García-Lario P., Acosta-Pulido J. A., Manchado A., Stanghellini L., Shaw R. A., Cataldo F., 2012, ApJ, 760, 107
Graczyk D. et al., 2014, ApJ, 780, 59
Herald J. E., Bianchi L., 2007, ApJ, 661, 845
Higdon S. J. U. et al., 2004, PASP, 116, 975
Hilditch R. W., Howarth I. D., Harries T. J., 2005, MNRAS, 357, 304
Hora J. L., Deutsch L. K., Hoffmann W. F., Fazio G. G., Shivanandan K., 1993, ApJ, 413, 304
Houck J. R. et al., 2004, ApJS, 154, 18
Howarth I. D., 1983, MNRAS, 203, 301
Hubeny I., 1988, Comput. Phys. Commun., 52, 103
Ishihara D., Kaneda H., Onaka T., Ita Y., Matsuura M., Matsunaga N., 2011, A&A, 534, A79
Kamath D., Wood P. R., Van Winckel H., 2014, MNRAS, 439, 2211
Karakas A. I., 2010, MNRAS, 403, 1413
Kingsburgh R. L., Barlow M. J., 1994, MNRAS, 271, 257
Kobayashi C., Karakas A. I., Umeda H., 2011, MNRAS, 414, 3231
Koller J., Kimeswenger S., 2001, ApJ, 559, 419
Kroto H. W., Heath J. R., Obrien S. C., Curl R. F., Smalley R. E., 1985, Nature, 318, 162
Kwok S., Hrivnak B. J., Su K. Y. L., 2000, ApJ, 544, L149
Lanz T., Hubeny I., 2003, ApJS, 146, 417
Leisy P., Dennefeld M., 2006, A&A, 456, 451
Lindsay E. M., 1961, AJ, 66, 169
Liu X.-W., 2006, in Barlow M. J., Méndez R. H., eds, Proc. IAU Symp. 234, Planetary Nebulae in Our Galaxy and Beyond. Cambridge Univ. Press, Cambridge, p. 219
Liu X.-W., Barlow M. J., Blades J. C., Osmer S., Clegg R. E. S., 1995, MNRAS, 276, 167
Liu X.-W., Storey P. J., Barlow M. J., Danziger I. J., Cohen M., Bryce M., 2000, MNRAS, 312, 585
Lodders K., 2010, in Goswami A., Reddy B. E., eds, Principles and Perspectives in Cosmochemistry. Springer-Verlag, Berlin, p. 379
Maas T., Van Winckel H., Lloyd Evans T., 2005, A&A, 429, 297
Mallik D. C. V., Peimbert M., 1988, Rev. Mex. Astron. Astrofis., 16, 111
Martin P. G., Rouleau F., 1991, in Malina R. F., Bowyer S., eds, Extreme Ultraviolet Astronomy. Pergamon Press, New York, p. 341
Mathis J. S., Rumpl W., Nordsieck K. H., 1977, ApJ, 217, 425
Meyssonnier N., Azzopardi M., 1993, A&AS, 102, 451
Morgan D. H., 1995, A&AS, 112, 445
Morisset C., Georgiev L., 2009, A&A, 507, 1517
Mucciarelli A., 2014, Astron. Nachr., 335, 79
Olive K. A., Skillman E. D., 2004, ApJ, 617, 29
Otsuka M., 2015, MNRAS, 452, 4070
Otsuka M., Tajitsu A., Hyung S., Izumiura H., 2010, ApJ, 723, 658
Otsuka M., Kemper F., Hyung S., Sargent B. A., Meixner M., Tajitsu A., Yanagisawa K., 2013, ApJ, 764, 77
Otsuka M., Kemper F., Cami J., Peeters E., Bernard-Salas J., 2014, MNRAS, 437, 2577
Otsuka M., Hyung S., Tajitsu A., 2015, ApJS, 217, 22
Peimbert M., Costero R., 1969, Bol. Obs. Tonantzintla Tacubaya, 5, 3
Peimbert M., Peimbert A., Ruiz M. T., 2000, ApJ, 541, 688
Peimbert M., Luridiana V., Peimbert A., 2007, ApJ, 666, 636
Phillips J. P., Sanchez Magro C., Martinez Roger C., 1984, A&A, 133, 395
Piskoti C., Yarger J., Zettl A., 1998, Nature, 393, 771
Prevot M. L., Lequeux J., Prevot L., Maurice E., Rocca-Volmerange B., 1984, A&A, 132, 389
Rieke G. H. et al., 2004, ApJS, 154, 25
Robbins R. R., 1968, ApJ, 151, 511
Ruffle P. M. E. et al., 2015, MNRAS, 451, 3504
Savage B. D., Mathis J. S., 1979, ARA&A, 17, 73
Scott A., Duley W. W., Pinho G. P., 1997a, ApJ, 489, L193
Scott A. D., Duley W. W., Jahani H. R., 1997b, ApJ, 490, L175
Seaton M. J., 1979, MNRAS, 187, 73p
Sellgren K., 1984, ApJ, 277, 623
Shaw R. A., Stanghellini L., Villaver E., Mutchler M., 2006, ApJS, 167, 201
Shaw R. A. et al., 2010, ApJ, 717, 562
Skrutskie M. F. et al., 2006, AJ, 131, 1163
Sloan G. C. et al., 2014, ApJ, 791, 28
Stanghellini L., Blades J. C., Osmer S. J., Barlow M. J., Liu X.-W., 1999, ApJ, 510, 687
Stanghellini L., Shaw R. A., Balick B., Mutchler M., Blades J. C., Villaver E., 2003, ApJ, 596, 997
Stanghellini L., Lee T.-H., Shaw R. A., Balick B., Villaver E., 2009, ApJ, 702, 733
Storey P. J., Hummer D. G., 1995, MNRAS, 272, 41
Subramanian S., Subramaniam A., 2009, A&A, 496, 399
Trams N. R., Waters L. B. F. M., Waelkens C., Lamers H. J. G. L. M., van der Veen W. E. C. J., 1989, A&A, 218, L1
Trams N. R., Waters L. B. F. M., Lamers H. J. G. L. M., Waelkens C., Geballe T. R., The P. S., 1991, A&AS, 87, 361
Tsamis Y. G., Barlow M. J., Liu X.-W., Danziger I. J., Storey P. J., 2003, MNRAS, 345, 186
Tsamis Y. G., Barlow M. J., Liu X.-W., Storey P. J., Danziger I. J., 2004, MNRAS, 353, 953
van Winckel H., 2003, ARA&A, 41, 391
Vassiliadis E., Wood P. R., 1994, ApJ, 92, 125
Vassiliadis E. et al., 1998, ApJS, 114, 237
Vernet J. et al., 2011, A&A, 536, A105
Villaver E., Stanghellini L., Shaw R. A., 2004, ApJ, 614, 716
Wesson R., Liu X.-W., Barlow M. J., 2005, MNRAS, 362, 424
Whittet D. C. B., ed., 2003, Dust in the Galactic Environment. IoP Publishing, Bristol
Zaritsky D., Harris J., Thompson I. B., Grebel E. K., Massey P., 2002, AJ, 123, 855
Zhang Y., Liu X.-W., 2003, A&A, 404, 545
Zhang Y., Liu X.-W., Liu Y., Rubin R. H., 2005, MNRAS, 358, 457
Zhen J., Castellanos P., Paardekooper D. M., Linnartz H., Tielens A. G. G. M., 2014, ApJ, 797, L30

APPENDIX A: COMMENTS ON ELEMENTAL ABUNDANCE DERIVATIONS USING ICFS

A1 He abundance

We removed the enhancement of the He I triplet by collisional excitation from the 2^3S level to derive He^+/H^+. Within their uncertainties, we do not find significant differences between He^+/H^+ derived from the triplet 10 830 Å and from other triplet lines except for He I 12 528 Å (see below), which indicates a small radiative transfer effect (e.g. Robbins 1968; Benjamin, Skillman & Smits 2002; Olive & Skillman 2004) in the lower transition lines [i.e. τ(He I 3889 Å) would be small]. Therefore, we do not correct the radiative transfer effect for triplets. The abundance result obtained from the He I 12 528 Å is below the 3σ limit from the average He^+/H^+ abundance (possibly due to the earth atmospheric

absorption correction). Therefore, we exclude this result when calculating the adopted He^+ abundance.

Estimating the He elemental abundance is not straightforward. Its derivation with the usage of the ICF(He) = $(S^+ + S^{2+})/S^{2+}$, proposed by Zhang & Liu (2003) for a low-excitation PN M2-24, provides ϵ(He) = 10.46, which is 1.6 lower than the predictions for the SMC primordial helium abundance (e.g. $Y_p = 0.2477 \pm 0.0029$, corresponding to ϵ(He)$\sim$10.9; Peimbert, Luridiana & Peimbert 2007). This inconsistent result indicates that the He^0 abundance has not been satisfactorily taken into account by this approach.

To overcome this problem, we tested the ICF(He) = $2.37 \cdot (S/S^{2+})$. This ICF(He) was determined by the P-I model of M1-11, and is a consequence of the prediction that the respective fractions of the He^+ and S^{2+} to He and S in M1-11 are 0.352 and 0.832. The selection of the S and S^{2+} abundances to correlate with the He and He^+ abundances was based on the fact that the ionization potential of S^{2+} is close to that of He^+. The usage of this ICF(He) (3.81 ± 0.22) improved our results, leading to 10.83 ± 0.03. Here, we derived the S abundance using equation 12 of Wesson, Liu & Barlow (2005) as follows. We obtain ICF(S) = 1.0,

$$\frac{S}{H} = \mathrm{ICF(S)} \cdot \left(\frac{S^+}{H^+} + \frac{S^{2+}}{H^+} \right),$$

$$\mathrm{ICF(S)} = \left[1 - \left(1 - \frac{O^+}{O} \right)^3 \right]^{-1/3}. \quad \text{(A1)}$$

From all elements in the neutral stage, helium is the one with the highest ionization potential, $\gtrsim 24$ eV. Even a small difference in the $T_{\rm eff}$ of the central star of Lin49 in comparison to the central star of M1-11 can lead to very different fractions of He^0 and He^+ in each PN. Therefore, we should treat ϵ(He) = 10.83 ± 0.03 as a lower limit for the He abundance.

Finally, we tested the ICF(He) used in H II regions ionized by soft radiation sources, as written by Peimbert & Costero (1969) as

$$\frac{He}{H} = \left(0.13 \frac{O}{O - O^+} + 0.87 \frac{S}{S - S^+} \right) \cdot \frac{He^+}{H^+}. \quad \text{(A2)}$$

Here, the O elemental abundance is the sum of the O^+ and O^{2+} abundances, and we excluded the neutral O abundance from the elemental O abundance. Equation (A2) gives ϵ(He) = 10.99 ± 0.02, where the term in parentheses corresponds to ICF(He) = 5.53 ± 0.14. This seems to be a much more reasonable He abundance result for an SMC PN, as it is comparable to the median value amongst the 14 SMC PNe analysed by Shaw et al. (2010, ϵ(He) = 11.11) and it is higher than ϵ(He) = 10.90, which is the mean He abundance of the SMC H II regions compiled by Shaw et al. (2010) based on the results of Dennefeld (1989). Thus, we adopt a range from 10.80 to 11.01 for the value of ϵ(He).

A2 N, Ne, Cl, Ar, and Fe abundances

We exclude the neutral N abundance from the elemental N abundance. The ICF(N) and N abundance were derived by Delgado-Inglada et al. (2014) from

$$\mathrm{N} = \mathrm{ICF(N)} \cdot \frac{N^+}{H^+},$$

$$\mathrm{ICF(N)} = 10^{0.64\omega} \cdot \frac{O}{O^+}. \quad \text{(A3)}$$

while the P-I model of M1-11 indicates

$$\mathrm{ICF(N)} = 1.14 \cdot \frac{O}{O^+}. \quad \text{(A4)}$$

The ICF(N)s given by equations (A3) and (A4) are very similar, 1.08 ± 0.04 and 1.18 ± 0.05, respectively. For Lin49, we adopt the ICF(N) calculated by equation (A3).

The ICFs of Ne, Cl, and Ar are based on the P-I model of M1-11 (Otsuka et al. 2013). Following this model, the Ne and Cl elemental abundances are derived as

$$\mathrm{Ne} = \mathrm{ICF(Ne)} \cdot \frac{Ne^+}{H^+},$$

$$\mathrm{Cl} = \mathrm{ICF(Cl)} \cdot \left(\frac{Cl^+}{H^+} + \frac{Cl^{2+}}{H^+} \right). \quad \text{(A5)}$$

The model predicts an Ne^+ fraction of 0.995, which supports the adopted ICF(Ne) = 1.0. The predicted fractions of Cl^+ and Cl^{2+} (0.169 and 0.832, respectively) were consistent with those of S^+ and S^{2+}. Since we confirm that the ICF(S) = 1.0 in Lin49, we also adopt a value equal to unity for ICF(Cl).

With the similarity of the Cl^{2+} and Ar^{2+} ionization potentials and the predicted fraction of Ar^{2+} (0.308), we adopt

$$\mathrm{ICF(Ar)} = 2.7 \cdot \frac{Cl}{Cl^{2+}},$$

$$\mathrm{Ar} = \mathrm{ICF(Ar)} \cdot \frac{Ar^{2+}}{H^+}. \quad \text{(A6)}$$

Finally, from the P-I model of M1-11, we obtain the following expression for the Fe elemental abundance:

$$\mathrm{ICF(Fe)} = 1.02 \cdot \frac{O}{O^+},$$

$$\mathrm{Fe} = \mathrm{ICF(Fe)} \cdot \frac{Fe^{2+}}{H^+}, \quad \text{(A7)}$$

which gives ICF(Fe) = 1.05 ± 0.04. This result is similar to the one given by the ICF(Fe) from Delgado-Inglada & Rodríguez (2014):

$$\mathrm{ICF(Fe)} = 0.9 \cdot \left(\frac{O^+}{O^{2+}} \right)^{0.08} \cdot \frac{O}{O^+}, \quad \text{(A8)}$$

which gives ICF(Fe) = 1.22 ± 0.05. We adopt the latter ICF(Fe) in the present work.

APPENDIX B: TABLES

Table B1. The detected and identified emission lines in the VLT/XSHOOTER spectrum of Lin49.

$\lambda_{obs.}$ (Å)	$\lambda_{lab.}$ (Å)	$f(\lambda)$	Ion	$I(\lambda)$ ($I(H\beta) = 100$)	$\delta I(\lambda)$	$\lambda_{obs.}$ (Å)	$\lambda_{lab.}$ (Å)	$f(\lambda)$	Ion	$I(\lambda)$ ($I(H\beta) = 100$)	$\delta I(\lambda)$	$\lambda_{obs.}$ (Å)	$\lambda_{lab.}$ (Å)	$f(\lambda)$	Ion	$I(\lambda)$ ($I(H\beta) = 100$)	$\delta I(\lambda)$
3662.97	3661.25	0.335	H31	0.199	0.021	6315.25	6312.10	−0.264	[S III]	0.306	0.010	8708.09	8703.87	−0.564	[Ni II]	0.022	0.003
3664.07	3662.26	0.335	H30	0.252	0.023	6350.26	6347.10	−0.269	Si II	0.111	0.017	8716.13	8711.70	−0.565	N I	0.020	0.006
3665.27	3663.40	0.335	H29	0.312	0.022	6366.98	6363.78	−0.271	[O I]	0.537	0.014	8731.47	8727.12	−0.566	[C I]?	0.036	0.005
3666.53	3664.68	0.334	H28	0.346	0.031	6551.39	6548.04	−0.296	[N II]	16.754	0.300	8754.93	8750.47	−0.568	P12	1.014	0.032
3667.95	3666.09	0.334	H27	0.492	0.030	6566.12	6562.80	−0.298	H3	284.700	4.423	8867.31	8862.78	−0.578	P11	1.287	0.038
3669.53	3667.68	0.334	H26	0.705	0.035	6581.36	6578.05	−0.300	C II	0.261	0.008	9019.51	9014.91	−0.590	P10	1.742	0.053
3671.26	3669.46	0.334	H25	0.751	0.041	6586.78	6583.46	−0.300	[N II]	50.106	0.844	9073.62	9068.60	−0.594	[S III]	2.680	0.090
3673.31	3671.48	0.333	H24	0.814	0.038	6681.56	6678.15	−0.313	He I	0.920	0.019	9222.94	9218.25	−0.604	Mg II	0.036	0.006
3675.55	3673.76	0.333	H23	0.895	0.038	6719.86	6716.44	−0.318	[S II]	1.749	0.030	9233.76	9229.01	−0.605	P9	2.208	0.070
3678.09	3676.36	0.332	H22	1.006	0.145	6734.24	6730.81	−0.320	[S II]	3.450	0.058	9248.79	9244.26	−0.606	Mg II	0.058	0.008
3681.07	3679.35	0.332	H21	1.203	0.169	7005.70	7002.12	−0.356	O I	0.192	0.006	9535.88	9530.60	−0.625	[S III]	5.950	0.200
3684.66	3682.81	0.331	H20	1.277	0.150	7068.81	7065.18	−0.364	He I	1.640	0.033	9550.86	9545.97	−0.626	P8	2.949	0.096
3688.69	3686.83	0.330	H19	1.463	0.138	7103.36	7099.80	−0.369	[Pb II]?	0.074	0.004	9829.20	9824.13	−0.643	[C I]	0.051	0.009
3693.33	3691.55	0.329	H18	1.608	0.152	7139.42	7135.80	−0.374	[Ar III]	0.788	0.023	9855.19	9850.26	−0.644	[C I]	0.110	0.009
3698.94	3697.15	0.328	H17	1.759	0.138	7234.77	7231.33	−0.387	C II	0.074	0.013	10 032.74	10 027.72	−0.655	He I	0.047	0.008
3705.63	3703.85	0.327	H16	1.888	0.174	7240.11	7236.42	−0.387	C II	0.170	0.010	10 054.52	10 049.37	−0.656	P7	4.325	0.147
3713.76	3711.97	0.325	H15	1.970	0.134	7258.02	7254.38	−0.390	O I	0.103	0.011	10 293.30	10 286.73	−0.668	[S II]	0.300	0.034
3723.76	3721.94	0.323	H14	2.849	0.148	7285.09	7281.35	−0.393	He I	0.231	0.010	10 343.05	10 336.41	−0.671	[S II]	0.329	0.025
3727.88	3726.03	0.322	[O II]	112.976	3.685	7322.91	7318.92	−0.398	[O II]	3.248	0.120	10 377.16	10 370.49	−0.673	[S II]	0.156	0.028
3730.63	3728.81	0.322	[O II]	51.359	1.890	7323.90	7319.99	−0.398	[O II]	6.491	0.158	10 404.42	10 397.74	−0.674	[N I]	0.051	0.015
3736.20	3734.37	0.321	H13	3.078	0.155	7333.45	7329.66	−0.400	[O II]	4.046	0.107	10 611.83	10 605.00	−0.684	Ca I?	0.116	0.009
3751.99	3750.15	0.317	H12	3.695	0.173	7334.55	7330.73	−0.400	[O II]	3.471	0.085	10 660.29	10 653.04	−0.687	N I?	0.036	0.015
3772.45	3770.63	0.313	H11	4.473	0.184	7446.02	7442.30	−0.415	N I	0.049	0.005	10 837.35	10 829.89	−0.695	He I	29.610	0.733
3799.74	3797.90	0.307	H10	5.862	0.262	7472.13	7468.31	−0.418	N I	0.073	0.004	10 945.37	10 938.10	−0.700	P6	8.927	0.273
3837.23	3835.38	0.299	H9	7.508	0.261	7755.07	7751.10	−0.455	[Ar III]	0.176	0.007	12 296.82	12 288.69	−0.751	C II?	0.029	0.010
3890.88	3889.05	0.286	H8	13.409	0.400	7820.14	7816.13	−0.464	He I	0.019	0.002	12 336.58	12 328.40	−0.752	Fe I	0.038	0.006
3920.73	3918.97	0.279	C II	0.105	0.015	8220.45	8215.90	−0.513	N II	0.061	0.004	12 389.56	12 381.63	−0.754	N I?	0.035	0.013
3922.48	3920.68	0.279	C II	0.189	0.018	8246.37	8242.39	−0.516	N I	0.071	0.005	12 535.55	12 527.49	−0.759	He I	0.074	0.007
3966.61	3964.73	0.267	He I	0.212	0.022	8247.89	8243.69	−0.516	P43	0.027	0.003	12 574.74	12 566.50	−0.760	Si III?	0.057	0.012
3971.99	3970.07	0.266	H7	16.743	0.463	8249.89	8245.64	−0.516	P42	0.042	0.003	12 742.46	12 733.89	−0.765	Fe II]?	0.149	0.022
4028.11	4026.18	0.251	He I	0.288	0.039	8251.95	8247.73	−0.516	P41	0.057	0.003	12 793.08	12 784.91	−0.766	He I	0.167	0.033
4070.56	4068.60	0.239	[S II]	1.689	0.055	8254.21	8249.97	−0.517	P40	0.054	0.008	12 798.77	12 790.35	−0.767	He I	0.065	0.034
4078.32	4076.35	0.237	[S II]	0.581	0.022	8256.41	8252.40	−0.517	P39	0.034	0.006	12 826.31	12 818.08	−0.767	P5	16.370	0.579
4103.70	4101.73	0.230	H6	26.380	0.614	8259.19	8255.02	−0.517	P38	0.058	0.006	13 173.28	13 164.55	−0.777	Ca I?	0.570	0.021
4269.24	4267.26	0.180	C II	0.121	0.018	8262.09	8257.85	−0.517	P37	0.057	0.005	14 857.58	14 848.14	−0.816	Br30	0.043	0.010
4289.33	4287.39	0.173	[Fe II]	0.128	0.012	8265.09	8260.93	−0.518	P36	0.063	0.007	14 921.34	14 911.45	−0.818	Br27	0.045	0.011
4342.53	4340.46	0.157	H5	46.910	0.773	8268.59	8264.28	−0.518	P35	0.088	0.008	14 947.28	14 937.73	−0.818	Br26	0.064	0.011
4361.46	4359.33	0.151	[Fe II]	0.064	0.012	8272.03	8267.94	−0.519	P34	0.058	0.005	14 977.28	14 967.33	−0.819	Br26	0.070	0.012
4365.29	4363.21	0.149	[O III]	0.145	0.012	8276.12	8271.93	−0.519	P33	0.069	0.009	15 010.76	15 000.86	−0.819	Br24	0.091	0.014
4389.95	4387.93	0.142	He I	0.066	0.007	8280.64	8276.31	−0.520	P32	0.071	0.009	15 143.43	15 133.22	−0.822	Br21	0.113	0.008
4473.62	4471.47	0.115	He I	0.964	0.028	8285.29	8281.12	−0.520	P31	0.091	0.015	15 201.58	15 191.84	−0.823	Br20	0.062	0.013
4573.19	4571.10	0.084	Mg I]?	0.175	0.010	8290.73	8286.43	−0.521	P30	0.101	0.013	15 270.63	15 260.54	−0.824	Br19	0.124	0.010
4660.31	4658.05	0.058	[Fe III]	0.091	0.008	8296.46	8292.31	−0.521	P29	0.107	0.015	15 351.91	15 341.79	−0.826	Br18	0.119	0.008
4715.38	4713.20	0.042	He I	0.070	0.007	8303.07	8298.83	−0.522	P28	0.108	0.011	15 448.82	15 438.92	−0.828	Br17	0.172	0.010
4863.62	4861.33	0.000	H4	100.000	1.029	8310.36	8306.11	−0.523	P27	0.126	0.010	15 566.22	15 556.45	−0.830	Br16	0.115	0.011
4883.55	4881.00	−0.005	[Fe III]	0.053	0.007	8318.35	8314.26	−0.524	P26	0.122	0.010	15 710.86	15 700.66	−0.832	Br15	0.256	0.014
4924.21	4921.93	−0.016	He I	0.212	0.012	8327.67	8323.42	−0.525	P25	0.131	0.014	15 891.00	15 880.54	−0.835	Br14	0.205	0.020
4961.25	4958.91	−0.026	[O III]	5.367	0.075	8338.03	8333.78	−0.526	P24	0.185	0.015	16 119.79	16 109.31	−0.839	Br13	0.402	0.020
5009.20	5006.84	−0.038	[O III]	15.996	0.311	8349.84	8345.55	−0.527	P23	0.173	0.012	16 417.76	16 407.19	−0.844	Br12	0.502	0.026
5018.03	5015.68	−0.040	He I	0.603	0.014	8363.28	8359.00	−0.529	P22	0.195	0.013	16 668.39	16 657.53	−0.847	Ca I?	0.058	0.018
5043.35	5041.02	−0.046	Si II	0.087	0.011	8378.74	8374.48	−0.531	P21	0.205	0.016	16 817.58	16 806.52	−0.850	Br11	0.658	0.029
5058.43	5055.98	−0.050	Si II	0.115	0.010	8396.70	8392.40	−0.533	P20	0.246	0.016	17 373.85	17 362.11	−0.857	Br10	0.910	0.050
5200.38	5197.90	−0.082	[N I]	0.130	0.023	8417.63	8413.32	−0.535	P19	0.274	0.018	17 432.15	17 429.49	−0.858	Mg I]?	0.268	0.031
5202.72	5200.26	−0.083	[N I]	0.060	0.011	8442.22	8437.95	−0.537	P18	0.316	0.015	19 457.63	19 445.56	−0.881	Br8	1.122	0.050
5272.88	5270.40	−0.098	[Fe III]	0.059	0.007	8450.77	8446.48	−0.538	O I	1.750	0.048	20 595.26	20 581.28	−0.891	He I	1.003	0.048
5301.44	5298.83	−0.104	[Fe II]	0.050	0.007	8471.60	8467.25	−0.541	P17	0.359	0.015	20 640.28	20 626.70	−0.892	Si I?	0.164	0.036
5540.35	5537.89	−0.149	[Cl III]	0.056	0.011	8506.86	8502.48	−0.544	P16	0.442	0.015	21 669.28	21 655.29	−0.900	Br7	2.752	0.123
5698.76	5695.92	−0.175	C III	0.206	0.021	8549.75	8545.38	−0.549	P15	0.523	0.017						
5757.49	5754.64	−0.185	[N II]	1.241	0.047	8583.08	8578.69	−0.552	[Cl II]	0.115	0.006						
5878.61	5875.60	−0.203	He I	3.772	0.044	8602.77	8598.39	−0.554	P14	0.661	0.023						
5961.53	5958.54	−0.215	O I	0.133	0.016	8669.44	8665.02	−0.560	P13	0.847	0.026						
5981.85	5978.93	−0.218	Si II	0.051	0.015	8684.69	8680.53	−0.562	Ca III	0.043	0.005						
6049.37	6046.44	−0.228	O I	0.139	0.011	8687.91	8683.40	−0.562	N I	0.034	0.005						
6303.48	6300.30	−0.263	[O I]	1.608	0.026	8690.65	8686.15	−0.562	N I	0.014	0.004						

Table B2. The adopted T_e and n_e pairs for each ionic abundance derivation.

T_e	n_e	Ions
T_e([S II])	n_e([S II])	N^0, O^0, S^+
T_e(PJ)	10 000 cm^{-3}	C^{2+}
T_e([O II])	n_e([O II])	O^+
T_e([S III])	n_e([O II])	Ne^+, S^{2+}, Cl^{2+}, Ar^{2+}
10 860 ± 210[a] K	n_e([O II])	Fe^{2+}, Cl^+
T_e([O III])	n_e([O II])	O^{2+}
11 360 ± 840[b] K	10 000 cm^{-3}	He^+
T_e([N II])	n_e([O II])	N^+

[a]The average value between T_e([O II]) and T_e([N II]).
[b]The average value between two T_e(He I) derived from the He I I(7281 Å)/I(6678 Å) and I(6678 Å/I(5876 Å).

Table B3. Ionic and elemental abundances derived from RLs and CELs. The ICF means the ionization correction factor for the unseen ionization stage ions in the XSHOOTER and *Spitzer*/IRS spectra. The ICF(He) determined based on the P-I model of M1-11 is 3.81 ± 0.22, leading to He/H = 6.73(−2) ± 4.29(−3).

Elem. (X)	Ion (X^{m+})	$\lambda_{lab.}$ (Å or μm)	$I(\lambda_{lab.})$ [I(Hβ) = 100]	X^{m+}/H$^+$	Elem. (X)	Ion (X^{m+})	$\lambda_{lab.}$ (Å or μm)	$I(\lambda_{lab.})$ [I(Hβ) = 100]	X^{m+}/H$^+$
He	He^+	3964.73	2.12(−1) ± 2.20(−2)	1.79(−2) ± 2.14(−3)	O	O^{2+}	4363.21	1.45(−1) ± 1.23(−2)	4.03(−6) ± 8.04(−7)
		4471.47	9.64(−1) ± 2.77(−2)	1.83(−2) ± 4.10(−3)			4958.91	5.37(+0) ± 7.45(−2)	3.90(−6) ± 3.54(−7)
		4921.93	2.12(−1) ± 1.24(−2)	1.55(−2) ± 1.32(−3)			5006.84	1.60(+1) ± 3.11(−1)	4.03(−6) ± 3.69(−7)
		5015.68	6.03(−1) ± 1.39(−2)	1.94(−2) ± 1.22(−3)					**3.97(−6) ± 2.43(−7)**
		5875.60	3.77(+0) ± 4.40(−2)	2.39(−2) ± 5.60(−3)				ICF(O)	1
		6678.15	9.20(−1) ± 1.88(−2)	2.29(−2) ± 1.58(−3)					**1.28(−4) ± 3.66(−6)**
		7281.35	2.31(−1) ± 1.03(−2)	2.02(−2) ± 1.38(−3)	Ne	Ne^+	12.81	1.12(+1) ± 1.16(+0)	1.49(−5) ± 1.56(−6)
		10829.9	2.96(+1) ± 7.33(−1)	1.57(−2) ± 1.05(−3)				ICF(Ne)	1
		12527.5	7.44(−2) ± 7.13(−3)	4.47(−2) ± 4.87(−3)					**1.49(−5) ± 1.56(−6)**
		12784.9	1.67(−1) ± 3.30(−2)	2.33(−2) ± 5.11(−3)	S	S^+	4068.60	1.69(+0) ± 5.47(−2)	4.22(−7) ± 7.03(−8)
		12790.4	6.46(−2) ± 3.38(−2)	2.74(−2) ± 1.45(−2)			4076.35	5.81(−1) ± 2.24(−2)	4.47(−7) ± 7.51(−8)
		20581.3	9.98(−1) ± 4.83(−2)	1.45(−2) ± 1.21(−3)			6716.44	1.75(+0) ± 3.00(−2)	3.94(−7) ± 9.92(−9)
				1.77(−2) ± 4.93(−4)			6730.81	3.45(+0) ± 5.83(−2)	3.92(−7) ± 6.74(−9)
			ICF(He)	5.53 ± 0.14			10286.7	3.00(−1) ± 3.39(−2)	3.20(−7) ± 6.36(−8)
				9.78(−2) ± 3.63(−3)			10336.4	3.29(−1) ± 2.52(−2)	3.56(−7) ± 6.43(−8)
C	C^{2+}	3918.97	1.05(−1) ± 1.53(−2)	5.31(−3) ± 3.51(−3)			10370.5	1.56(−1) ± 2.77(−2)	3.54(−7) ± 8.57(−8)
		3920.68	1.89(−1) ± 1.85(−2)	5.31(−3) ± 9.59(−4)					**3.92(−7) ± 5.49(−9)**
		4267.26	1.21(−1) ± 1.82(−2)	1.17(−4) ± 2.29(−5)		S^{2+}	6312.10	3.06(−1) ± 1.05(−2)	6.44(−7) ± 6.41(−8)
		6578.05	2.61(−1) ± 7.61(−3)	3.36(−4) ± 5.32(−5)			9068.60	2.68(+0) ± 8.97(−2)	6.43(−7) ± 3.57(−8)
		7236.42	1.70(−1) ± 9.54(−3)	2.32(−4) ± 3.64(−5)					**6.43(−7) ± 3.12(−8)**
		7231.33	7.41(−2) ± 1.25(−2)	1.82(−4) ± 4.06(−5)				ICF(S)	1
				1.17(−4) ± 2.29(−5)					**1.04(−6) ± 3.17(−8)**
			ICF(C)	3.96 ± 0.23	Cl	Cl^+	8578.69	1.15(−1) ± 5.52(−3)	4.50(−9) ± 2.72(−10)
				4.62(−4) ± 9.43(−5)		Cl^{2+}	5537.89	5.65(−2) ± 1.12(−2)	6.32(−9) ± 1.31(−9)
N	N^0	5197.90	1.30(−1) ± 2.33(−2)	6.15(−7) ± 1.12(−7)				ICF(Cl)	1
		5200.26	5.96(−2) ± 1.15(−2)	6.63(−7) ± 1.28(−7)					**1.08(−8) ± 1.33(−9)**
		10397.7	5.11(−2) ± 1.48(−2)	5.75(−7) ± 2.10(−7)	Ar	Ar^{2+}	7135.80	7.88(−1) ± 2.33(−2)	6.77(−8) ± 3.92(−9)
				6.28(−7) ± 7.81(−8)			7751.10	1.76(−1) ± 7.03(−3)	6.32(−8) ± 4.03(−9)
	N^+	5754.64	1.24(+0) ± 4.66(−2)	7.29(−6) ± 9.10(−7)					**6.69(−8) ± 3.94(−9)**
		6548.04	1.68(+1) ± 3.00(−1)	7.18(−6) ± 2.45(−7)				ICF(Ar)	4.62 ± 1.11
		6583.46	5.01(+1) ± 8.44(−1)	7.25(−6) ± 2.43(−7)					**3.03(−7) ± 7.48(−8)**
				7.22(−6) ± 1.70(−7)	Fe	Fe^{2+}	4658.05	9.13(−2) ± 7.78(−3)	2.95(−8) ± 2.76(−9)
			ICF(N)	1.08 ± 0.04			4881.00	5.35(−2) ± 6.97(−3)	2.38(−8) ± 3.58(−9)
				7.80(−6) ± 3.69(−7)			5270.40	5.94(−2) ± 7.23(−3)	3.92(−8) ± 4.98(−9)
O	O^0	6300.30	1.61(+0) ± 2.55(−2)	5.30(−6) ± 1.25(−6)					**2.92(−8) ± 2.00(−9)**
		6363.78	5.37(−1) ± 1.42(−2)	5.53(−6) ± 1.31(−6)				ICF(Fe)	1.22 ± 0.05
				5.41(−6) ± 9.03(−7)					**3.57(−8) ± 2.85(−9)**
	O^+	3726.03	1.13(+2) ± 3.68(+0)	1.23(−4) ± 4.30(−6)					
		3728.81	5.14(+1) ± 1.89(+0)	1.23(−4) ± 8.70(−6)					
		7318.92	3.25(+0) ± 1.20(−1)	1.76(−4) ± 3.16(−5)					
		7319.99	6.49(+0) ± 1.58(−1)	1.14(−4) ± 1.99(−5)					
		7329.66	4.05(+0) ± 1.07(−1)	1.33(−4) ± 2.35(−5)					
		7330.73	3.47(+0) ± 8.53(−2)	1.16(−4) ± 2.03(−5)					
				1.24(−4) ± 3.65(−6)					

Table B4. Comparison between SED modellings and observations. In the third and eighth columns, the predicted values by the single-shell model as we discussed in Section 3.4 are given. The values in the fourth and ninth columns are the predictions by the two-shell model in Section 4.1.2.

Ion	$\lambda_{lab.}$	I(ModelS) [$I(H\beta) = 100$]	I(ModelT) [$I(H\beta) = 100$]	I(Obs) [$I(H\beta) = 100$]	Ion	$\lambda_{lab.}$	I(ModelS) [$I(H\beta) = 100$]	I(ModelT) [$I(H\beta) = 100$]	I(Obs) [$I(H\beta) = 100$]
[O III]	1661/65 Å	0.077	0.091	–	[Ar III]	7135 Å	0.766	0.773	0.788
N III]	1747/49 Å	0.251	0.242	–	He I	7281 Å	0.245	0.242	0.231
C III]	1906/09 Å	49.742	49.380	–	[O II]	7323 Å	10.961	10.811	9.740
[C II]	2326 Å	182.426	184.421	–	[O II]	7332 Å	8.754	8.635	7.517
[O II]	2471 Å	14.829	14.627	–	[Ar III]	7751 Å	0.185	0.186	0.176
[O II]	3726 Å	140.734	138.440	112.976	[Cl II]	8579 Å	0.114	0.113	0.115
[O II]	3729 Å	68.410	67.314	51.359	[S II]	9069 Å	4.269	4.249	2.680
He I	3965 Å	0.331	0.330	0.212	[S II]	1.029 μm	0.280	0.279	0.300
[S II]	4070 Å	1.198	1.197	1.689	[S II]	1.034 μm	0.274	0.274	0.329
[S II]	4078 Å	0.388	0.387	0.581	[S II]	1.037 μm	0.131	0.131	0.156
H I	4102 Å	26.729	26.739	26.380	H I	1.094 μm	9.069	9.009	8.927
C II	4267 Å	0.073	0.072	0.121	He I	1.253 μm	0.068	0.071	0.074
H I	4340 Å	47.483	47.500	46.910	He I	1.278 μm	0.191	0.190	0.167
[O III]	4363 Å	0.122	0.185	0.145	He I	1.279 μm	0.064	0.063	0.065
He I	4388 Å	0.156	0.155	0.066	H I	1.282 μm	16.126	16.125	16.370
He I	4471 Å	1.249	1.243	0.964	H I	1.736 μm	0.929	0.930	0.910
[Fe III]	4659 Å	0.110	0.106	0.091	He I	2.058 μm	1.137	1.121	0.998
[Fe III]	4881 Å	0.040	0.039	0.053	H I	2.166 μm	2.742	2.743	2.752
He I	4922 Å	0.337	0.335	0.212	[Ar II]	6.99 μm	1.320	1.352	–
[O III]	4959 Å	4.703	4.779	5.367	H I	7.46 μm	2.562	2.561	–
[O III]	5007 Å	14.155	14.384	15.996	[Ar III]	9.00 μm	0.626	0.623	–
He I	5016 Å	0.817	0.812	0.603	[S IV]	10.52 μm	0.019	0.018	–
[N I]	5198 Å	0.028	0.028	0.130	H I	11.31 μm	0.311	0.310	–
[N I]	5200 Å	0.017	0.017	0.060	H I	12.37 μm	0.992	0.991	–
[Fe III]	5271 Å	0.062	0.060	0.059	[Ne II]	12.81 μm	12.645	14.168	11.157
[Cl III]	5538 Å	0.080	0.078	0.056	[Ne III]	15.55 μm	0.068	0.079	–
[N II]	5755 Å	1.127	1.127	1.241	[S III]	18.67 μm	3.958	3.913	–
He I	5876 Å	3.305	3.799	3.772	H I	19.06 μm	0.438	0.437	–
[O I]	6300 Å	1.367	1.374	1.608	[S III]	33.47 μm	1.341	1.326	–
[S III]	6312 Å	0.352	0.352	0.306	[Ne III]	36.01 μm	0.005	0.006	–
[O I]	6363 Å	0.436	0.438	0.537	[O III]	51.80 μm	0.902	0.821	–
[N II]	6548 Å	19.214	19.164	16.754	[N III]	57.21 μm	0.273	0.259	–
H I	6563 Å	286.554	286.602	284.700	[O I]	63.17 μm	0.211	0.212	–
[N II]	6584 Å	56.701	56.552	50.106	[O III]	88.33 μm	0.146	0.133	–
He I	6678 Å	1.025	1.018	0.920	[N II]	121.7 μm	0.108	0.108	–
[S II]	6716 Å	1.881	1.879	1.749	[O I]	145.5 μm	0.012	0.012	–
[S II]	6731 Å	3.325	3.319	3.450	[C II]	157.6 μm	0.722	0.724	–
He I	7065 Å	1.550	1.576	1.431	[N II]	205.4 μm	0.012	0.012	–

Band	λ_c	I(ModelS) [$I(H\beta) = 100$]	I(ModelT) [$I(H\beta) = 100$]	I(Obs) [$I(H\beta) = 100$]	X	$\epsilon(X)_{ModelS}$	$\epsilon(X)_{ModelT}$	$\epsilon(X)_{Obs}$
MCPSV	5450 Å	42.396	46.315	38.095	He	10.80	10.80	10.80–11.01
2MAJ	1.235 μm	61.385	91.351	96.770	C	8.46	8.46	8.46
2MAH	1.662 μm	31.233	131.036	114.920	N	7.06	7.06	6.93
2MAK	2.159 μm	20.788	156.257	139.370	O	8.03	8.03	8.11
IRA3	3.600 μm	28.570	251.534	236.040	Ne	7.22	7.27	7.18
IRA4	4.500 μm	37.205	191.422	240.080	S	5.88	5.88	6.02
LIS1	15.00 μm	36.248	36.749	44.550	Cl	4.09	4.08	4.03
LIS2	23.35 μm	64.739	63.899	53.290	Ar	5.21	5.22	5.48
LIS3	36.50 μm	26.733	26.192	24.710	Fe	4.79	4.71	4.55

Band	λ_c	F_ν(ModelS) (mJy)	F_ν(ModelT) (mJy)	F_ν(Obs) (mJy)
FIT1	65.00 μm	9.255	9.023	7.415
FIT2	90.00 μm	3.419	3.331	4.470
FIT3	120.0 μm	1.400	1.366	2.465

Table B5. Effective temperature of the central star ($T_{\rm eff}$), nebular radius (r), and nebular elemental abundances in non-C_{60}-containing C-rich PNe in the SMC. We recalculated the C in SMC17 using the F([C III] 1906/09 Å) and F(Hβ) of Aller et al. (1987), c(Hβ), $T_{\rm e}$([O III]) = 12 200 K, and $n_{\rm e}$ = 2900 cm^{-3} of Shaw et al. (2010), and the ICF(C) = O/O^{2+} derived from the elemental O and ionic O^{2+} abundances of Shaw et al. (2010).

Non-C_{60} PNe	$T_{\rm eff}$ (K)	r (arcsec)	ϵ(He)	ϵ(C)	ϵ(N)	ϵ(O)	ϵ(Ne)	ϵ(S)	ϵ(Ar)	References
SMC2	111 500	0.25	11.10	8.74	7.47	8.01	7.21	7.32	5.78	(1),(2),(3),(4)
SMC5	137 500	0.31	11.11	8.68	7.76	8.24	7.43	7.68	6.01	(1),(3),(5),(6)
SMC6	28 200	0.19	10.99	8.35	8.06	7.99	7.14	7.37	5.70	(1),(7),(8),(9)
SMC11	40 900	0.99	11.01	–	6.52	8.02	6.90	6.28	5.97	(7),(10),(9)
SMC14	83 500	0.42	11.13	9.16	7.36	8.29	7.65	>6.27	5.82	(1),(7),(9),(10)
SMC17	58 400	0.25	11.14	8.63	7.38	8.21	7.67	>6.15	5.56	(4),(7),(9),(10),(11)
SMC19	59 400	0.30	11.09	8.97	7.28	8.19	7.62	>6.05	5.54	(1),(7),(9),(10)
SMC20	86 500	0.15	11.14	8.25	6.95	7.74	6.91	5.67	5.03	(7),(8),(9),(10)
SMC27	43 300	0.23	10.99	8.58	7.55	8.03	7.03	5.84	5.32	(7),(9),(10),(12)
Average	72 100	0.34	11.08	8.67	7.37	8.08	7.28	6.69	5.64	

References – (1) Leisy & Dennefeld (2006) for abundances; (2) Shaw et al. (2006) for r; (3) Liu et al. (1995) for $T_{\rm eff}$; (4) Aller et al. (1987); (5) Vassiliadis et al. (1998) for the C/O ratio of 2.779 in SMC5; (6) Stanghellini et al. (1999) for r; (7) Stanghellini et al. (2003) for r; (8) Stanghellini et al. (2009) for C; (9) Villaver et al. (2004) for $T_{\rm eff}$; (10) Shaw et al. (2010) for abundances except C; (11) this work; (12) Tsamis et al. (2003) for abundances except S.

This paper has been typeset from a TEX/LATEX file prepared by the author.